Journal Pre-proof

Spatially developing supersonic turbulent boundary layer subjected to static surface deformations

Vilas Shinde, Aaron Becks, Rohit Deshmukh, Jack McNamara, Datta Gaitonde, Mallory Neet, Joanna Austin

PII: S0997-7546(21)00101-1
DOI: https://doi.org/10.1016/j.euromechflu.2021.07.002
Reference: EJMFLU 103804

To appear in: *European Journal of Mechanics / B Fluids*

Received date : 10 February 2021
Revised date : 24 June 2021
Accepted date : 6 July 2021

Please cite this article as: V. Shinde, A. Becks, R. Deshmukh et al., Spatially developing supersonic turbulent boundary layer subjected to static surface deformations, *European Journal of Mechanics / B Fluids* (2021), doi: https://doi.org/10.1016/j.euromechflu.2021.07.002.

Spatially developing supersonic turbulent boundary layer subjected to static surface deformations

Vilas Shinde, Aaron Becks, Rohit Deshmukh, Jack McNamara*, Datta Gaitonde

Department of Mechanical and Aerospace Engineering, The Ohio State University, Columbus - OH 43210, USA

Mallory Neet, Joanna Austin

Graduate Aerospace Laboratories, California Institute of Technology, Pasadena, CA 91125

Abstract

The effects of static surface deformations on a spatially developing supersonic boundary layer flow at Mach number $M = 4$ and Reynolds number $Re_{\delta_{in}} \approx 49300$, based on inflow boundary layer thickness (δ_{in}), are analyzed by performing large eddy simulations. Two low-order structural modes of a rectangular clamped surface panel of dimensions $\approx 33\delta_{in} \times 48\delta_{in}$ are prescribed with modal amplitudes of δ_{in}. The effects of these surface deformations are examined on the boundary layer, including changes in the mean properties, thermal and compressibility effects and turbulence structure. The results are analyzed in the context of deviations from concepts typically derived and employed for equilibrium turbulence. The surface deflections, to some degree, modify the correlations that govern both Morkovin's hypothesis and strong Reynolds analogy away from the wall, whereas in the near-wall region both the hypotheses breakdown. Modifications to the turbulence structure due to the surface deformations are elucidated by means of the wall pressure two-point correlations and anisotropy invariant maps. In addition to the amplification of turbulence, such surface deformations lead to local flow separation, instigating low-frequency unsteadiness. One consequence of significance to practical design is the presence of low frequency unsteadiness similar to that encountered in impinging or ramp shock boundary layer interactions.

Keywords: supersonic turbulent boundary layer, compressible turbulence, fluid-structure interaction

1. Introduction

Significant progress has been made in understanding of supersonic turbulent boundary layers, as documented in classical experimental [1, 2, 3] as well as recent computational [4, 5, 6, 7] efforts. The canonical flat plate configuration has defined important attributes inherent to equilibrium turbulent boundary layers. While turbulence generation is a major focus area in subsonic turbulent boundary layers, supersonic counterparts include several other complicating factors, including the effects of the compressibility, boundary layer growth, and temperature on the turbulence structure [8]. Common simplifications invoked in high-speed turbulent wall-bounded layers in mechanical equilibrium include Morkovin's hypothesis and the strong Reynolds analogy (SRA), where the fluctuations of the total temperature are assumed to be negligible; this facilitates the adoption of various aspects of the more commonly examined subsonic turbulence dynamics [9, 10, 11]. These hypotheses are reasonable if the fluctuating Mach number or equivalently the density and temperature fluctuations remain small: for boundary layers, this condition is typically assumed

*Corresponding author
Email address: mcnamara.190@osu.edu (Jack McNamara)

to hold if the flow Mach number is less than five. However, for flows of practical interest, which typically undergo strong pressure gradients and are no longer in equilibrium, the above approximations, and associated simplifications, may no longer hold.

The imposition of strong pressure gradients on a supersonic turbulent boundary layer leads to enhanced compressibility effects, dramatically modifying the flow turbulence [12, 13]. Several parameters govern such flows, including Mach and Reynolds numbers, pressure and thermal field gradients and surface geometry, complicating prediction of the state of the boundary layer [8]. Canonical supersonic flows that include pressure gradients have been examined in recent experiments [14] as well as with direct numerical simulations (DNS) and large eddy simulations (LES) [15, 16, 17]. Adverse/favorable pressure gradients can arise due to many factors, including surface curvatures (concave/convex), wall heating gradients and shock wave boundary layer interactions. Experimental and theoretical studies have gained insight into the separate effects of each of these. For example, adverse pressure gradients and concave wall curvature destabilize the boundary layer and enhance turbulent mixing, in terms of the conservation of angular momentum [3, 18]. The destabilization manifests as an increase in the turbulent fluctuations due to streamline curvature, adverse pressure gradients and bulk compression [19, 20]. This contrasts with the stabilizing effects of favorable pressure gradients, which include weakening of coherent structures [21, 22] and lead to a decrease in the turbulence, particularly in the outer region of the boundary layer [23]. The effects of pressure gradient and surface curvature also manifest into the friction velocity and wall friction, which vary inversely due to the flow compressibility, as elucidated by Wang et al. [24] by carefully analyzing the modification of principal strain rate.

In the present work, we consider the effect on turbulence of statically deformed rectangular panels that comply with basic modes arising commonly in fluid-structure interactions (FSI). This effectively breaks down the fully coupled problem into a geometrically simpler variant that isolates some of the crucial effects of surface deformations on the evolution of turbulent boundary layers and enables a better understanding of fully coupled interactions such as those being performed experimentally by Neet and Austin [25]. To this end, a rectangular panel is statically deformed in its fundamental modes of vibration, namely, Mode(1,1) and Mode(2,1). The notation Mode(a,b) follows the convention that the first entry ('a') corresponds to the wave number in the streamwise direction (two times the number of cycles per unit panel length) and the second term ('b') corresponds to the wave number in the spanwise direction (two times the number of cycles per unit panel width). For concreteness, the geometric and flow parameters are chosen to be similar to those of Neet and Austin [25]. Thus, the aspect ratio of the panel is fixed at 1.377 (the ratio of the spanwise to streamwise lengths), with modal deformation amplitude of 2.5% of the panel streamwise length, which equals the inflow boundary layer thickness (δ_{in}). These parameters generate a suitable response in the boundary layer, and simplify the task of identifying the impact of pressure gradients imposed by static surface deformations on the supersonic turbulent boundary layer. The specific areas of focus are turbulence structure, thermal and compressibility effects and flow unsteadiness, with results being placed in the context of various findings in the literature. The article is arranged as follows: Sec. 2 provides the numerical methodology and the experimental and numerical flow configuration details. The results, Sec. 3, are divided into Sec. 3.1, which presents variations in boundary layer quantities of practical interest, such as the skin-friction, the wall pressure and wall temperature, Sec. 3.2 on flow compressibility, Sec. 3.3 on turbulence structure and Sec. 3.4 on flow unsteadiness. Lastly, the findings are summarized in Sec. 4.

2. Numerical set-up

2.1. Flow governing equations

The governing full 3-D compressible Navier-Stokes equations are solved in curvilinear coordinates, $(x, y, z, t) \rightarrow (\xi, \eta, \zeta, \tau)$ with $t = \tau$ using the strong conservation form:

$$\frac{\partial}{\partial \tau}\left(\frac{\vec{U}}{J}\right) + \frac{\partial \hat{F}}{\partial \xi} + \frac{\partial \hat{G}}{\partial \eta} + \frac{\partial \hat{H}}{\partial \zeta} = \frac{1}{Re}\left[\frac{\partial \hat{F}_v}{\partial \xi} + \frac{\partial \hat{G}_v}{\partial \eta} + \frac{\partial \hat{H}_v}{\partial \zeta}\right] \tag{1}$$

where $\vec{U} = [\rho, \rho u, \rho v, \rho w, \rho E]^T$ is the conserved solution vector. Here u, v and w are the Cartesian components of the velocity, while ρ is the density and E is the internal energy. $J = \partial(\xi, \eta, \zeta, \tau)/\partial(x, y, z, t)$ denotes the transformation Jacobian. The flow variables are non-dimensionalized by their reference (∞) values, except for pressure, which is normalized by $\rho_\infty u_\infty^2$. The length scale is considered to be the panel length in the streamwise direction (a), which is 40 times the boundary layer thickness at the domain inflow (δ_{in}); thus, $Re_a = \rho_\infty u_\infty a/\mu_\infty$.

The inviscid fluxes $\hat{F}, \hat{G}$ and $\hat{H}$ can be given as,

$$\hat{F} = \frac{1}{J}\begin{bmatrix} \rho U \\ \rho u U + \xi_x p \\ \rho v U + \xi_y p \\ \rho w U + \xi_z p \\ (\rho E + p)U - \xi_t p \end{bmatrix}, \hat{G} = \frac{1}{J}\begin{bmatrix} \rho V \\ \rho u V + \eta_x p \\ \rho v V + \eta_y p \\ \rho w V + \eta_z p \\ (\rho E + p)V - \eta_t p \end{bmatrix}, \hat{H} = \frac{1}{J}\begin{bmatrix} \rho W \\ \rho u W + \zeta_x p \\ \rho v W + \zeta_y p \\ \rho w W + \zeta_z p \\ (\rho E + p)W - \zeta_t p \end{bmatrix}. \tag{2}$$

U, V and W are the contravariant velocity components:

$$U = \xi_t + \xi_x u + \xi_y v + \xi_z w, \tag{3}$$

$$V = \eta_t + \eta_x u + \eta_y v + \eta_z w, \tag{4}$$

$$W = \zeta_t + \zeta_x u + \zeta_y v + \zeta_z w, \tag{5}$$

$$\text{and} \quad E = \frac{T}{\gamma(\gamma-1)M_\infty^2} + \frac{1}{2}\left(u^2 + v^2 + w^2\right), \tag{6}$$

where T, γ and M_∞ are the temperature, ratio of specific heats and reference Mach number respectively. The ratio of specific heats for air is assumed to be $\gamma = 1.4$.

The viscous fluxes $\hat{F}_v, \hat{G}_v$ and $\hat{H}_v$ are:

$$\hat{F}_v = \frac{1}{J}\begin{bmatrix} 0 \\ \xi_x\tau_{xx} + \xi_y\tau_{xy} + \xi_z\tau_{xz} \\ \xi_x\tau_{xy} + \xi_y\tau_{yy} + \xi_z\tau_{yz} \\ \xi_x\tau_{xz} + \xi_y\tau_{yz} + \xi_z\tau_{zz} \\ \xi_x b_x + \xi_y b_y + \xi_z b_z \end{bmatrix}, \hat{G}_v = \frac{1}{J}\begin{bmatrix} 0 \\ \eta_x\tau_{xx} + \eta_y\tau_{xy} + \eta_z\tau_{xz} \\ \eta_x\tau_{xy} + \eta_y\tau_{yy} + \eta_z\tau_{yz} \\ \eta_x\tau_{xz} + \eta_y\tau_{yz} + \eta_z\tau_{zz} \\ \eta_x b_x + \eta_y b_y + \eta_z b_z \end{bmatrix}, \hat{H}_v = \frac{1}{J}\begin{bmatrix} 0 \\ \zeta_x\tau_{xx} + \zeta_y\tau_{xy} + \zeta_z\tau_{xz} \\ \zeta_x\tau_{xy} + \zeta_y\tau_{yy} + \zeta_z\tau_{yz} \\ \zeta_x\tau_{xz} + \zeta_y\tau_{yz} + \zeta_z\tau_{zz} \\ \zeta_x b_x + \zeta_y b_y + \zeta_z b_z \end{bmatrix}, \tag{7}$$

where, with index notation $x_i(\equiv x, y, z)$, $\xi_i(\equiv \xi, \eta, \zeta)$ and $u_i(\equiv u, v, w)$,

$$b_{x_i} = u_j \tau_{x_i x_j} - \dot{q}_{x_i} \tag{8}$$

$$\tau_{x_i x_j} = \mu\left(\frac{\partial \xi_k}{\partial x_j}\frac{\partial u_i}{\partial \xi_k} + \frac{\partial \xi_k}{\partial x_i}\frac{\partial u_j}{\partial \xi_k}\right) + \lambda_b \frac{\partial \xi_l}{\partial x_k}\frac{\partial u_k}{\partial \xi_l}\delta_{ij} \tag{9}$$

$$\dot{q}_{x_i} = -\left[\frac{\mu}{Pr(\gamma-1)M_\infty^2}\right]\frac{\partial \xi_j}{\partial x_i}\frac{\partial T}{\partial \xi_j}. \tag{10}$$

Here μ is the dynamic viscosity of the fluid. Stokes' hypothesis for the bulk viscosity $\lambda_b = -2/3\mu$ is assumed, while the change in fluid viscosity due to the temperature is modeled with Sutherland's law. The fluid is assumed to be a perfect gas, which leads to $p = \rho T/\gamma M_\infty^2$. A constant value of the Prandtl number, $Pr = 0.72$, is assumed.

The governing equations are solved with the second-order implicit time-marching scheme of Beam and Warming [26], with two Newton-like subiterations in order to reduce factorization and explicit boundary condition application errors. Further details on the time scheme are provided in Visbal and Gordnier [27]. The spatial derivative terms are discretized using a $6th$-order compact central finite difference scheme, ensuring no dissipation error on uniform meshes. A small value of artificial damping is added for numerical stability, similar to Shinde et al. [28, 29]. Detailed validation studies may be found in Visbal and Gaitonde [30], Gaitonde and Visbal [31], Visbal and Gaitonde [32], and Garmann [33]. In shock regions, which are detected by a simple switch for a specified threshold parameters [34], the high-order compact scheme is replaced by the classical Roe scheme with a 2^{nd} order reconstruction.

Flow										
	M_∞	Re $(/m)$	P_0 (N/m^2)	T_0 (K)	p_∞ (N/m^2)	u_∞ (m/s)	ρ_∞ (kg/m^3)	δ_{in} (mm)	δ_{LE} (mm)	δ_{TE} (mm)
	4	2.375×10^7	5×10^5	290	3.3×10^3	674	0.17	1.65	2.60	3.70
Panel										
	a	b/a	δ_{in}/a	Re_a	A_m/a					
	1	1.377	0.025	1.57×10^6	0.025					

Table 1: Flow and panel parameters

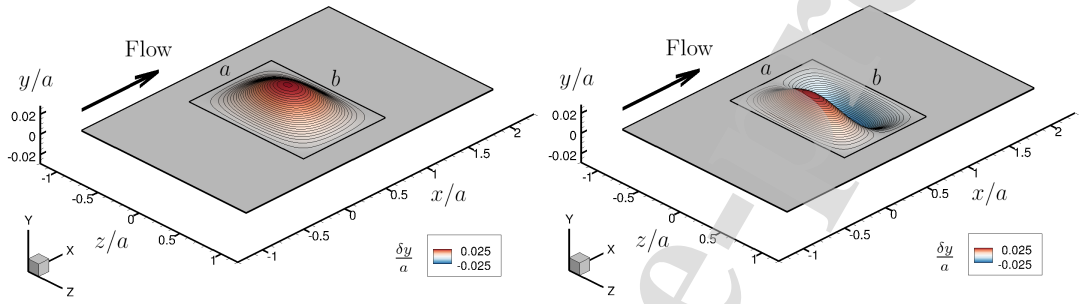

(a) Mode(1,1) (a) Mode(2,1)

Figure 1: Flow geometries with surface modal deformations: (a) Mode(1,1); (b) Mode(2,1).

2.2. Flow configuration

The flow parameters are shown in Table 1. The Mach number (4) and other choices reflect those achieved in the Caltech Ludwieg Tube [25], where fully coupled experiments are being conducted. Other attributes, including panel dimensions are presented in Table 1. Length scales are normalized by the streamwise length of the panel insert, a. Thus, the non-dimensional spanwise length of the panel insert (b/a) and inflow boundary layer thickness (δ_{in}/a) are 1.377 and 0.025, respectively, while the Reynolds number based on a is 1.57×10^6. The inflow boundary layer thickness is conveniently chosen to ensure a sufficient departure from the equilibrium state when subjected to surface deformations. The characterization of the inflow turbulent boundary layer, in terms of the boundary layer thickness and growth rate, is performed by means of the same boundary layer edge detection procedure on the time-averaged schlieren images (in experiments) and density gradient magnitude (in simulations) [25]. A verification study on the inflow boundary layer characterization indicate that the simulated values of the boundary layer thickness at the leading and trailing edges of the panel and the growth rate are within 2.7%, 5.2%, and 11% of the experimental values, respectively.

In addition to the flat plate base case, the deflected surfaces with Mode(1,1) and Mode(2,1) surface deformations are considered to investigate the effect of surface static deformation. The geometries of the modal surface deformations of Mode(1,1) and Mode(2,1) are displayed in Fig. 1(a) and Fig. 1(b), respectively, with the peak modal amplitude A_m/a for the both cases is 0.025. This value is sufficient to distort the boundary layer to an extent that facilitates extraction of trends relative to the flat plate, with Mode(2,1) imposing the distortion twice as rapidly as Mode(1,1).

The dimensions of the computational domain in the streamwise and spanwise directions are $L_x/a = 3$ and $L_z/a = 2$ for all three cases (Base, Mode(1,1), and Mode(2,1)). The computational domain extents are $-1 \leq x/a \leq 2$ and $-1 \leq z/a \leq 1$ in the streamwise and spanwise directions, respectively, as shown in Fig. 1; the panel extends $0 \leq x/a \leq 1$ streamwise and $-0.6889 \leq z/a \leq 0.6889$ spanwise. The domain length in the wall normal direction is $L_y/a = 1$ over $0 \leq y/a \leq 1$, which extends out in the negative y direction by $A_m/a = 0.025$ for Mode(2,1) (Fig. 1 b). The computational mesh size is based on numerous other efforts

at similar flow parameters, including coupled interactions [28, 35] and transitional and turbulent morphing studies [36, 37, 38]. The computational domain is discretized in $901 \times 283 \times 601$ grid-points in the streamwise (x), wall normal (y) and spanwise (z) directions, respectively, where the discretization is uniform in the x and z directions. The mesh, referred as $\mathcal{G}_1$, is stretched in the y-direction by using geometric progression with a growth rate of 1.03, where the first grid-point lies at a distance of 1.0×10^{-4} a from the wall, resulting in ≈ 115 grid points inside the boundary layer at the domain inflow. At the entrance to the domain, these results correspond to grid resolution of $\Delta x^+ = 31.7$, $\Delta y^+_{min} = 0.95$, $\Delta y^+_{\delta_{in}} = 3.92$, and $\Delta z^+ = 31.7$ in the wall units.

The flow turbulence at the inflow boundary is generated by the digital filter procedure originally proposed by Klein et al. [39]. Xu et al. [40] improved the method by limiting the filtering operation to a 2-D inflow plane, while using a temporal correlation function to avoid 3-D filtering. Furthermore, spatial auto-correlations are assumed to be exponential rather than Gaussian, which leads to better correlations for the dominant flow structures. Although DNS databases are often employed to obtain the time-mean velocity and Reynolds stresses, in the present work, such a database is not available. Thus, modeled statistics from a much cheaper Reynolds Averaged Navier-Stokes (RANS) simulation with a $k - \epsilon$ turbulence model is used, following the practices outlined by Adler et al. [41] to obtain an equilibrium turbulent boundary layer that interacts with the surface deformation. Far field boundary conditions are specified with first-order extrapolation of all variables on the downstream, top and side faces of the computational domain, while the bottom surface is a no-slip adiabatic wall.

The simulations are performed for a non-dimensional total time duration of $tu_\infty/a = 200$ for each case (Base, Mode(1,1) and Mode(2,1)) with a constant time-step of $\Delta t u_\infty/a = 0.001$. The initial transients die out by $tu_\infty/a = 40$, which is equivalent to ≈ 13 flow-through times; while the statistics are accumulated over ≈ 53 flow-through times, ensuring time-converged results.

To assess the mesh dependence of the results, we simulate the flat base case using a higher mesh resolution with reduced the spanwise and wall normal extents of the domain to $-0.1 \leq z/a \leq 0.1$ and $0 \leq y/a \leq 0.5$, respectively, while maintaining the streamwise domain size. The mesh $\mathcal{G}_2$ uses $1051 \times 221 \times 167$ grid-points in the streamwise, wall normal and spanwise directions, respectively, leading to increased spanwise resolution of $\Delta z^+ \approx 7.14$ in the wall units. The geometric progression in the wall normal direction uses a growth rate of 1.02, which results in $\Delta y^+_{min} = 0.5$ and $\Delta y^+_{\delta_{in}} = 3.98$ near the wall and edge of the boundary layer, respectively. Figure 2 displays the mesh sensitivity of results in terms of the van Driest transformed streamwise velocity and pertinent Reynolds stresses at a streamwise location $x/a = -0.35$, where the van Driest transformation and normalization in wall units is obtained by

$$\langle u \rangle^+_{VD} = \int_0^{\langle u \rangle^+} \sqrt{\frac{\langle \rho \rangle}{\langle \rho \rangle_w}} d\langle u \rangle^+ \qquad y^+ = \frac{y u_\tau}{\langle \mu/\rho \rangle_w} \qquad \langle u_i' u_j' \rangle^+ = \frac{\langle u_i' u_j' \rangle}{u_\tau^2}, \tag{11}$$

where u_τ is the friction velocity. The establishment of turbulent boundary layer downstream of the inflow can be compared with the near wall linear and logarithmic laws, respectively:

$$\langle u \rangle^+_{VD} = y^+ \quad \text{and} \quad \langle u \rangle^+_{VD} = \frac{1}{0.41} \ln(y^+) + 5.1. \tag{12}$$

In addition, the streamwise velocity and Reynolds stress profiles are compared with the DNS profiles of Bernardini and Pirozzoli [42] at Mach 4 and Reynolds number $Re_{\delta_{in}} = 83623$, which is approximately double the present case, providing an estimate of the departure from an equilibrium turbulent boundary layer.

For perspective, an instance of the turbulent boundary layer obtained through LES is shown in Fig. 3 with normalized density. The leading and trailing edges of the panel insert are indicated by the vertical dashed lines. The boundary layer thicknesses at these locations are $\delta_{LE}/a = 0.029$ and $\delta_{TE}/a = 0.045$, respectively. A three-dimensional (3-D) view of the spatially developing TBL for all cases is shown in Fig. 4 using Q-criterion isosurface colored by velocity magnitude. The figure clearly shows the influence of surface deformation on flow turbulence, including especially rapid changes in the form and density of hairpin like flow structures due to the panel deflection, as they grow along the positive streamwise direction. In addition,

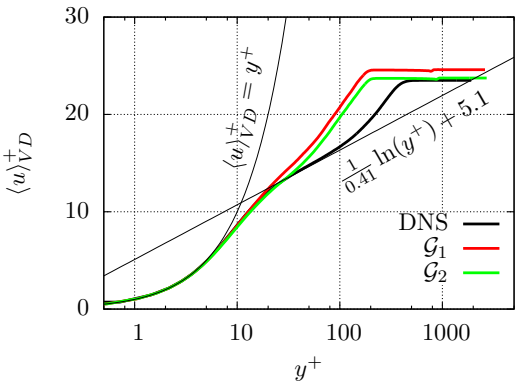

(a) van Driest transformed mean velocity

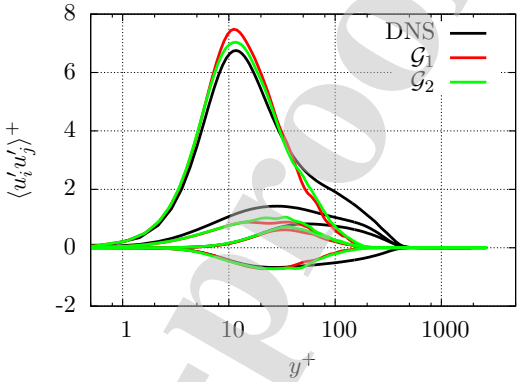

(b) Reynolds stresses (From top: $\langle u_1' u_1' \rangle^+$, $\langle u_3' u_3' \rangle^+$, $\langle u_2' u_2' \rangle^+$, and $\langle u_1' u_2' \rangle^+$)

Figure 2: Development of the inflow boundary layer at $x/a = -0.35$ against the fully developed DNS [42] profiles at Mach 4 and Reynolds number $Re_{\delta_{in}} = 83623$, or equivalently $Re_{\delta_{in}} \approx 4.181 \times 10^7$ $(/m)$.

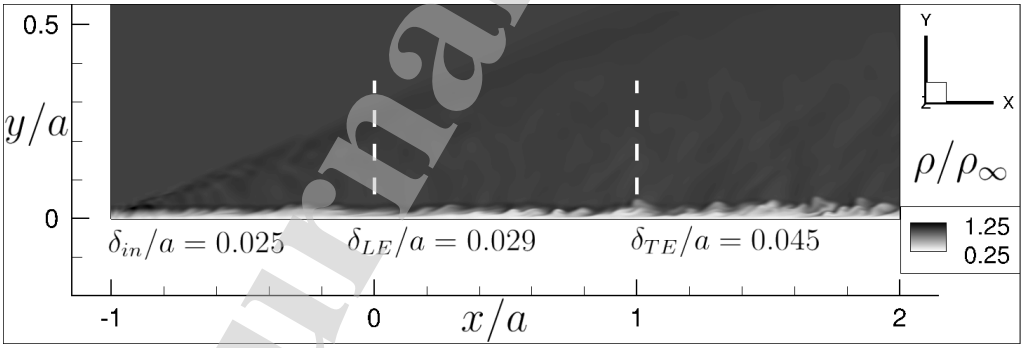

Figure 3: Instantaneous turbulent boundary layer over the flat plate model in terms of the normalized density (ρ/ρ_∞)

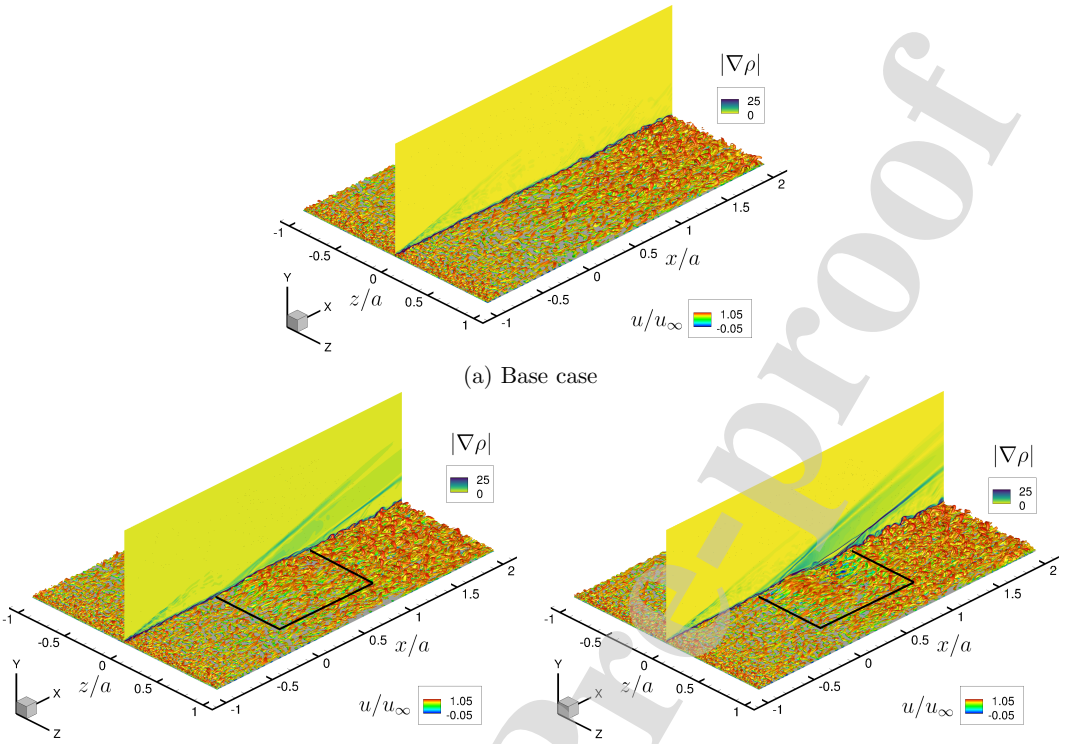

(a) Base case

(b) Mode(1,1)

(c) Mode(2,1)

Figure 4: Three dimensional flow structures, displaying a Q criterion isosurface colored with streamwise velocity, developing over the Mode(2,1) configuration. The compliant panel is delineated by the black rectangle.

the vertical spanwise mid-planes display the magnitude of density gradient, exhibiting the compression and expansion waves emanated due to the surface deformations. These effects depend on the specifics of the deflection, and are discussed further below.

3. Results and discussion

3.1. Modification of the boundary layer

In this section, we discuss the modification of the wall quantities of practical significance due to surface deformation in terms of the difference with respect to the baseline case. The time-mean wall pressure profiles $\Delta\langle p_w\rangle$ along the panel center-line ($z = 0$), normalized by the free-stream pressure $p_\infty = \rho_\infty u_\infty^2$, are displayed in Fig. 5(a) for the two cases: Mode(1,1) and Mode(2,1). As expected, the pressure profiles for the two cases are identical in the inlet region of the computational domain ($x/a \lessapprox -0.25$), whereas the pressure profiles are considerably modified over the surface deformations for both cases, before returning to zero difference with the baseline in the downstream region ($x/a \gtrapprox 1.25$). The effect of surface deflection is reflected on the wall pressure slightly upstream of the leading edge of the panel (Fig. 5a), indicating the flow deceleration in the upstream near-wall region of the deflection. The deviation in the wall pressure profile occurs at an upstream distance of $\approx 5\delta_{in}$ ($\approx 0.125a$) for Mode(1,1) and $\approx 10\delta_{in}$ ($\approx 0.25a$) for Mode(2,1) from the panel leading edge. Comparing the two cases, the upstream influence length appears to scale linearly with the surface curvature at the panel leading edge, which for Mode(2,1) is approximately twice that for Mode(1,1), where a higher surface curvature corresponds to a smaller radius of curvature. However, in general, effects of

the streamline curvature, compression and pressure gradient are closely related to each other and separating the influence of each is difficult [8]. The wall pressure profiles for Mode(1,1) and Mode(2,1), in Fig. 5(a), are modified with respect to the Base case over the streamwise extent of $-0.25 \lessapprox x/a \lessapprox 1.5$ due to the respective surface deflections of panel over $0 \leq x/a \leq 1$.

The modified wall pressure due to surface deflection is often estimated by means of simplified flow theories. For instance, for a surface deflection of δy, the time averaged wall pressure can be derived based on the second-order potential (quasi-steady supersonic) flow theory by Van Dyke [43] as:

$$\frac{\langle p_w(x)\rangle}{p_\infty} = \frac{1}{\sqrt{M_\infty^2 - 1}} \frac{d(\delta y)}{dx}, \tag{13}$$

The pressure profile for Mode(1,1) in Fig. 5(a) closely follows the profile of the gradient of surface deflection $d(\delta y)/dx$ as per Eq. 13, and it is also consistent with the correlation of streamwise gradients of the time-mean wall pressures, as shown in Fig. 5(b), to $d^2(\delta y)/dx^2$. However, significant deviations are evident from this correlation for Mode(2,1), most notably in areas corresponding to flow separation; this is consistent with the anticipated breakdown of simplified inviscid models for wall pressure in such regions. The modified time-averaged wall pressure profiles for the two cases along the spanwise direction at a streamwise location of $x/a = 0.75$ are displayed in Fig. 5(e).The wall pressures exhibit Gaussian-like profiles for both Mode(1,1) and Mode(2,1) in response to the corresponding surface deflections. The spanwise three-dimensionality introduced by Mode(1,1) and Mode(2,1) surface deflections is evident (Fig. 5e), where in general Mode (1,1) results in higher difference with the baseline, particularly at the centerline location ($z = 0$).

A measure of flow separation can be obtained by means of the skin-friction coefficient along the symmetry plane:

$$C_f = \frac{\langle \tau_w \rangle}{\frac{1}{2}\rho_\infty u_\infty^2} \quad \text{with} \quad \tau_w = \mu \left.\frac{du}{dy}\right|_w, \tag{14}$$

where τ_w is the local wall shear stress on the wall. The effect of surface deflection on the skin-friction coefficient is shown in Fig. 5(c), where the ΔC_f is the difference between the respective deflected case and the baseline. Similar to the wall pressure profiles, the difference of the skin-friction profiles for Mode(1,1) and Mode(2,1) deviate from the Base case at about $x/a \approx -0.25$ and reunite downstream approximately at $x/a \approx 1.5$. For Mode(2,1), the difference in the skin-friction coefficient (Fig. 5c) becomes negative at $x/a \approx 0.069$ and also near $x/a \approx 0.478$, indicating two distinct regions of flow separation. The flow separation and reattachment locations are denoted by S and R, respectively, on the figure (Fig. 5c). The locations of flow separation are consistent with the stronger pressure gradients induced by Mode(2,1) surface deflections. The first region of separation forms near the leading edge of the panel in $-0.069 \lessapprox x/a \lessapprox 0.1$ with a separation length of $L_{s1}/a \approx 0.169$; whereas the second region of separation arises in $0.478 \lessapprox x/a \lessapprox 0.812$ with a separation length of $L_{s2}/a \approx 0.334$. For Mode(1,1), on the other hand, the skin-friction coefficient remains positive, in the time mean sense; however, the value near the leading edge of panel is nearly zero, suggesting the time-localized presence of separation in the unsteady flow. The streamwise variations in the skin-friction coefficient for Mode(1,1) and Mode(2,1) follow the pattern that high values occur at streamwise locations where the wall pressure gradient is favorable, such as in the vicinity of the apexes of the surface deflections.

At constant Reynolds number and adiabatic conditions, generally, an increase in the Mach number leads to the increase of the near-wall temperature and decrease of the near-wall density, resulting in a decrease of the skin-friction coefficient [8]. The time-mean wall temperature for Mode(1,1) and Mode(2,1) relative to the Base case ($\Delta\langle T_w\rangle/T_\infty$) are displayed in Fig. 5(d). The wall temperatures exhibit local variations due surface deformations, which gradually relax to the Base case wall temperature in the downstream region ($x/a \gtrapprox 1.5$). These variations are, to some extent, associated with the rise and fall of the wall pressures in Fig. 5(a), as well as with the flow separation regions for Mode(2,1). In addition to the wall pressure gradient, the wall temperature and flow separation appear to affect the skin-friction coefficient, particularly for Mode(2,1), which leads to much higher flow separation and temperature in $0.5 \gtrapprox x/a \gtrapprox 1.0$. The spanwise mean wall temperature variation for the two cases is displayed in Fig. 5(f), clearly indicating the

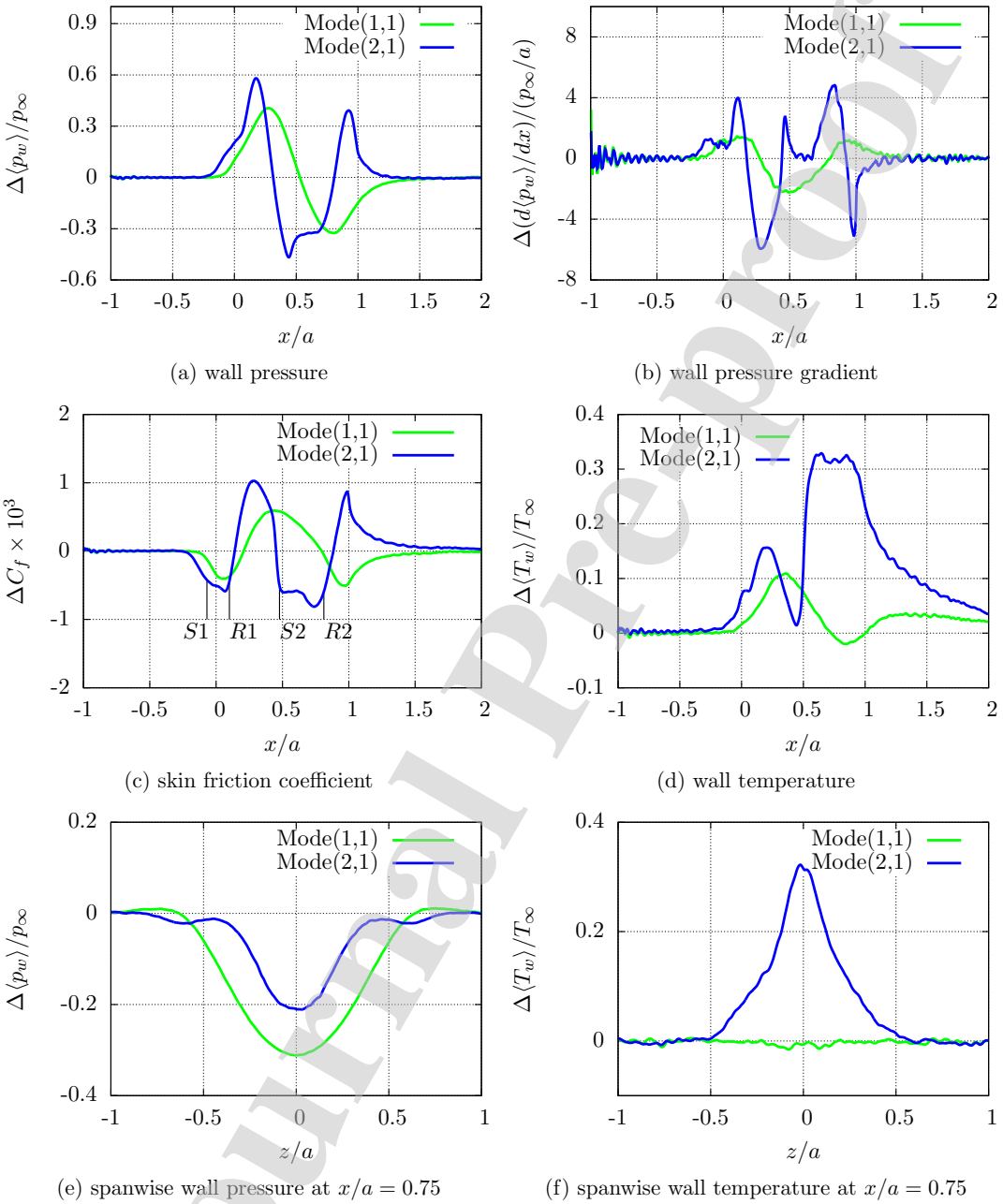

Figure 5: Comparison of the wall properties for the two cases (Mode(1,1) and Mode(2,1)) relative to the baseline. (a) Wall pressure, (b) wall pressure gradient, (c) skin friction coefficient, (d) wall temperature as function of streamwise location, (e) wall pressure along the span at $x/a = 0.75$ and (f) wall temperature along the span at $x/a = 0.75$.

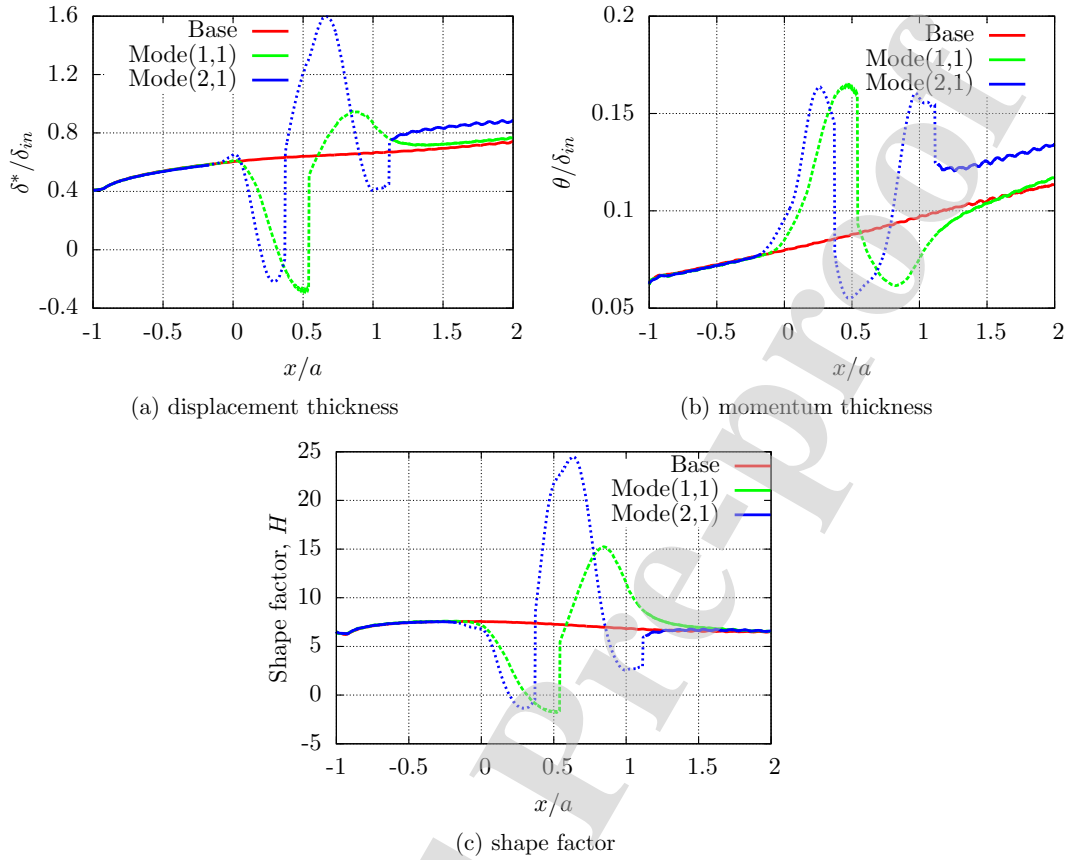

(a) displacement thickness

(b) momentum thickness

(c) shape factor

Figure 6: Streamwise evolution of the (a) displacement thickness, (b) momentum thickness, and (c) shape factor along the centerline $z = 0$ for the Base case, Mode(1,1) and Mode(2,1).

wall temperature rise for Mode(2,1) along $x/a = 0.75$ inside the separated flow with a peak at the centerline ($z/a = 0$).

The shape factor, H, of a boundary layer provides useful information about the state of the boundary layer [44], particularly when its susceptibility to separation under adverse pressure gradients [45].

$$H = \frac{\delta^*}{\theta} \qquad \delta^* = \int_0^{\delta_x} \left(1 - \frac{\rho u}{\rho_\infty u_\infty}\right) dy \qquad \theta = \int_0^{\delta_x} \frac{\rho u}{\rho_\infty u_\infty}\left(1 - \frac{u}{u_\infty}\right) dy, \tag{15}$$

where δ^* and θ are the displacement and momentum thicknesses of the boundary layer. A theoretical estimate of the shape factor of an equilibrium supersonic TBL may be obtained by using a power-law relation for the mean velocity of an incompressible TBL [46, 20]. For instance, $u/u_\infty = (y/\delta_x)^{1/n}$ gives the velocity profile of a zero pressure gradient incompressible TBL, where n weakly depends on the Reynolds number (Re_x). This leads to $H_i = (2 + n)/n$, where i stands for incompressible. Thus, for $n = 7$, the shape factor is $H_i \approx 1.26$. For a supersonic TBL over a flat surface with adiabatic wall condition, the shape factor can be expressed as, $H/H_i = 1 + r(\gamma - 1)M_\infty^2$, where r is the recovery factor [46]. For Mach number $M_\infty = 4$, the ratio of specific heats $\gamma = 1.4$ and the recovery factors of $r = 1$ and $r = 0.8$, the shape factor values are $H = 9.32$ and $H = 7.7$, respectively.

Figure 6 displays the variation of δ^*, θ and H with distance along the centerline ($z = 0$). Although the flow is not in equilibrium, particularly in locally separated regions, the integrations in Eq. 15 are nonetheless carried, estimating the local boundary layer thickness δ_x corresponding to $0.99u_\infty$. The profiles are significantly modified due to the presence of surface deformations in the Mode(1,1) and Mode(2,1). In general, a constant value of shape factor indicates a well-behaved zero pressure gradient turbulent boundary layer [44, 45]. The departure of profiles from equilibrium, due to surface deformation and/or pressure gradient, is marked by dashed lines in Fig. 6. The displacement thickness, in general, decreases for the positive slopes of surface deformation (concave curvature or compression effects) and vice versa; whereas the momentum thickness exhibits opposite trends, where it increases for the positive slopes of surface deformation and vice versa. Furthermore, the shape factor mainly follows the variations in the displacement thickness (Fig. 6 c).

Similar to the displacement thickness, the shape factor decreases over the compression surfaces and increases over the expansion surfaces, as shown in Fig. 6(c). The higher values of shape factor indicate the regions of higher adverse pressure gradient where the flow is prone to separation, but only over the expansion surfaces: $0.5 \leq x/a \leq 1$ for Mode(1,1) and $0.25 \leq x/a \leq 0.75$ for Mode(2,1). For instance, we can infer about the possibility of separation at $x/a \approx 0.8$ for Mode(1,1) and the occurrence of separation at $x/a \approx 0.6$ for Mode(2,1). The shape factor for the three cases converge to a constant value of $H \approx 6.6$ for $x/a \gtrapprox 1.5$, returning to equilibrium; however, the downstream evolution of the turbulent boundary layer influenced by the effects of surface deflection [47]. In addition, the shape factor informs the effects of surface deformations from the boundary layer stability point of view. The rise or fall of the shape factor, in Fig. 6(c), corresponds to de-stabilization or stabilization of the boundary layer, respectively. This is consistent with the fact that convex curvature stabilizes the boundary layer, whereas concave curvature destabilizes the boundary layer [48, 20]. Furthermore, after an initial adjustment, concave curvature leads to increase in the wall friction, heat transfer, and Reynolds stresses as well as it may give rise to Taylor-Görtler like vortices; on the other hand, the convex surface deformation typically results in opposite effects. The skin-friction and wall temperature of Fig. 5 are in agreement with these observations; however, the Taylor-Görtler like vortices, which contribute to enhancement of the flow turbulence, are not observed.

In addition to these opposite effects of the concave and convex curvatures, the supersonic TBL responds differently in the near-wall region as opposed to the outer region of boundary layer, in terms of the turbulence kinetic energy and mean streamwise velocity. However, for the present parameters, the effect of combinations of curvatures, such as in Mode(2,1), do not produce a linear superposition of the two; this contrasts with the linear superposition observed for a single surface curvature and a pressure gradient by Smith and Smits [49]. The boundary layers in Mode(1,1) and Mode(2,1), which are distorted due to the surface deformations, relax to an equilibrium state (zero pressure gradient state) at a distance of $\approx 0.5a$ ($\approx 20\delta_{in}$) downstream from the trailing edge of panel. The time-averaged streamwise velocity and Reynolds stresses at this location ($x/a = 1.5$) for the three cases are displayed in Fig. 7. The streamwise velocity for Mode(1,1) and Mode(2,1) exhibits a decrease and an increase respectively when compared to the Base case in $0 < y/\delta_{x/a=1.5} \lessapprox 0.2$, the near-wall region of the boundary layer; whereas in the outer region, the distorted profiles are nearly recovered (Fig. 7 a). The streamwise component of Reynolds stress tensor, $\langle u'u' \rangle / u_\infty^2$, exhibits a slight decrease in its peak values for both Mode(1,1) and Mode(2,1) compared to the Base case. On the other hand, the wall-normal ($\langle v'u' \rangle / u_\infty^2$), spanwise ($\langle w'w' \rangle / u_\infty^2$) and the off-diagonal $\langle u'v' \rangle / u_\infty^2$ components of the Reynolds stress tensor are significantly increased in the near-wall region, indicating an overall increase of the turbulent kinetic energy.

The strength of the boundary layer distortion can be quantified in terms of an additional strain rate, e, and the primary strain rate, $\partial\langle u \rangle / \partial y$ [10]. $e/(\partial\langle u \rangle / \partial y) \lessapprox 0.01$ and $e/(\partial\langle u \rangle / \partial y) \gtrapprox 0.01$ represent weak and strong distortion values, respectively. The primary strain rate provides the measure of eddy strain rate, estimated by $(-\langle u'v' \rangle)^{1/2}/L_\epsilon$, where u' and v' are the fluctuating streamwise and wall-normal components of velocity and L_ϵ is a dissipation length scale. The flow or eddy response time scale can be approximated by the turbulent kinetic energy (TKE) per unit rate of TKE production [50], and it is inversely proportional to the primary strain rate. Furthermore, the characteristic time scale of turbulence, T_t, can be also defined based on the integral length scale of turbulence (L_t) and the root mean squared (rms) velocity fluctuations u'_{rms} as, $T_t = L_t/u'_{rms}$ [51]. The distortion is termed as rapid when a characteristic time scale of the

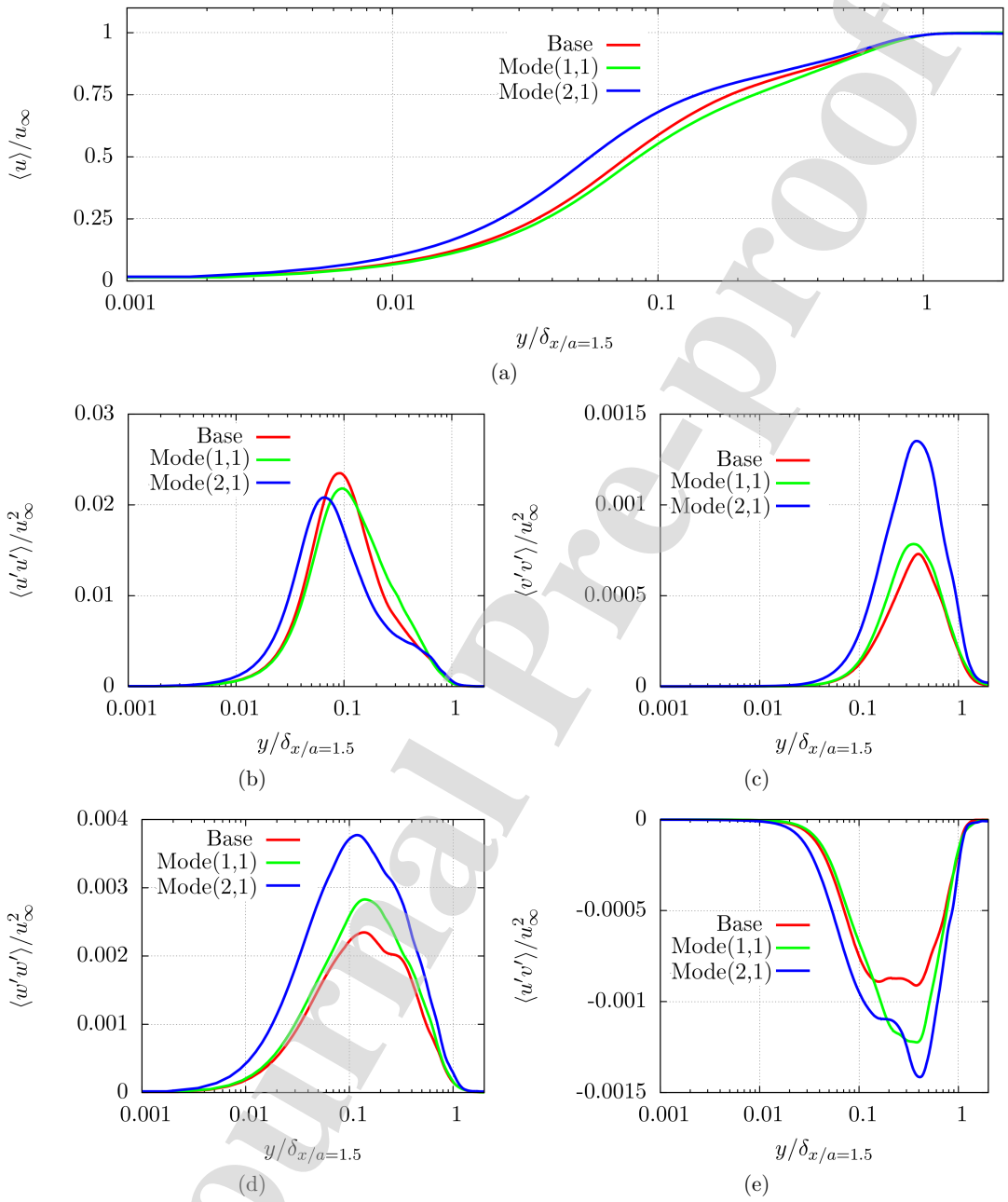

Figure 7: (a) Time-mean streamwise velocity and (b)-(e) Reynolds stresses a downstream location $x/a = 1.5$ for the three cases.

Loc.	$L1$	$L2$	$L3$	$L4$	$L5$
x/a	-0.5	0.0	0.5	1.0	1.5

Table 2: Streamwise reference locations on the wall surface ($y/a = 0$) along the domain centerline ($z/a = 0$).

turbulence (T_t) is much larger compared to the distortion time T_d, that is $T_d/T_t \ll 1$.

Rapid distortion theory (RDT) considerations [52, 53] can provide insights into the interpretation of the observations. The distortion time for the Mode(1,1) and Mode(2,1) can be estimated based on the streamwise lengths of $a/2$ and $a/4$ respectively and the sound velocity c; where the distortion length corresponds to the distance of the first peak of surface deflection from the panel leading edge. This results in the time scales of $T_d \approx 2$ and $T_d \approx 1$ for Mode(1,1) and Mode(2,1) respectively, where the values are also equal to the respective gradient Mach number. The integral length scale (L_t) of turbulence is typically associated with most energy producing turbulent eddies; for turbulent boundary layers, this length scale can be assumed to be δ, a local value of the boundary layer thickness. Thus the turbulence time scale is approximately $T_t \approx 0.2$, leading to $T_d/T_t \approx 10$ for Mode(1,1) and $T_d/T_t \approx 5$ for Mode(2,1). Evidently, the ratio T_d/T_t is much larger than 1 for both the cases, contrary to the assumption of $T_d/T_t \ll 1$ in the rapid distortion theory, indicating that the boundary layer distortions are not rapid.

3.2. Compressibility and thermal effects

The implications of panel deflections are now examined in the context of Morkovin's hypothesis [9], specifically that key features of incompressible turbulence persist in the supersonic regime ($1.5 \lessapprox M_\infty \lessapprox 5$) without significant modifications, other than mean density variation. Beyond $M_\infty \gtrapprox 5$, compressibility effects, in addition to the velocity and pressure fluctuations, density and temperature fluctuations may also affect the different mechanisms of energy exchange among the turbulence scales. The relations between the velocity and temperature fluctuations, encapsulated in the strong Reynolds analogy (SRA), can be considerably affected due to the higher levels of the acoustic and thermal fluctuations.

The turbulent Mach number,

$$M_t = \frac{\sqrt{\langle u_i' u_i' \rangle}}{\langle c \rangle}. \tag{16}$$

often employed with a threshold of $M_t \approx 0.3$ for the appearance of compressibility effects on turbulence [20], is plotted Fig. 8 at the different streamwise locations of Table 2. For all cases and locations, the turbulent Mach number is lower than the threshold of 0.3 for compressibility, indicating, in the equilibrium case, the applicability of Morkovin's hypothesis and strong Reynolds analogy by this measure. The analysis was also be conducted in terms of the fluctuating Mach number (M_f), which takes into account the variation in the speed of sound [8]:

$$M_f = \sqrt{\langle M^2 \rangle - \langle M \rangle^2}. \tag{17}$$

The results were again analyzed at locations ($L2$, $L3$, $L4$ and $L5$) (not included for brevity). The maximum values of M_f in all cases remain less than the threshold of 0.3 considered necessary to manifest the special effects of compressibility on turbulence. Although the profiles for Mode(1,1) and Mode(2,1) deviate from the Base case in the region of the panel, particularly at the mid-chord ($L3$) and trailing edge ($L4$) locations (see Fig. 8), they recover relatively rapidly towards the Base case profile within half the panel length downstream, by location $L5$.

We now examine the effect of the panel distortion on interactions between the thermal and velocity fluctuations, which are typically assumed small for equilibrium boundary layers when $1.5 \lessapprox M_\infty \lessapprox 5$. The relevant parameter is the turbulent Prandtl number Pr_t, which is the ratio of turbulent momentum to turbulent heat diffusivities. Typical considerations assume a Pr_t of unity for Reynolds analogy considerations to derive the correspondence between velocity and temperature profiles. The assumption of negligible total

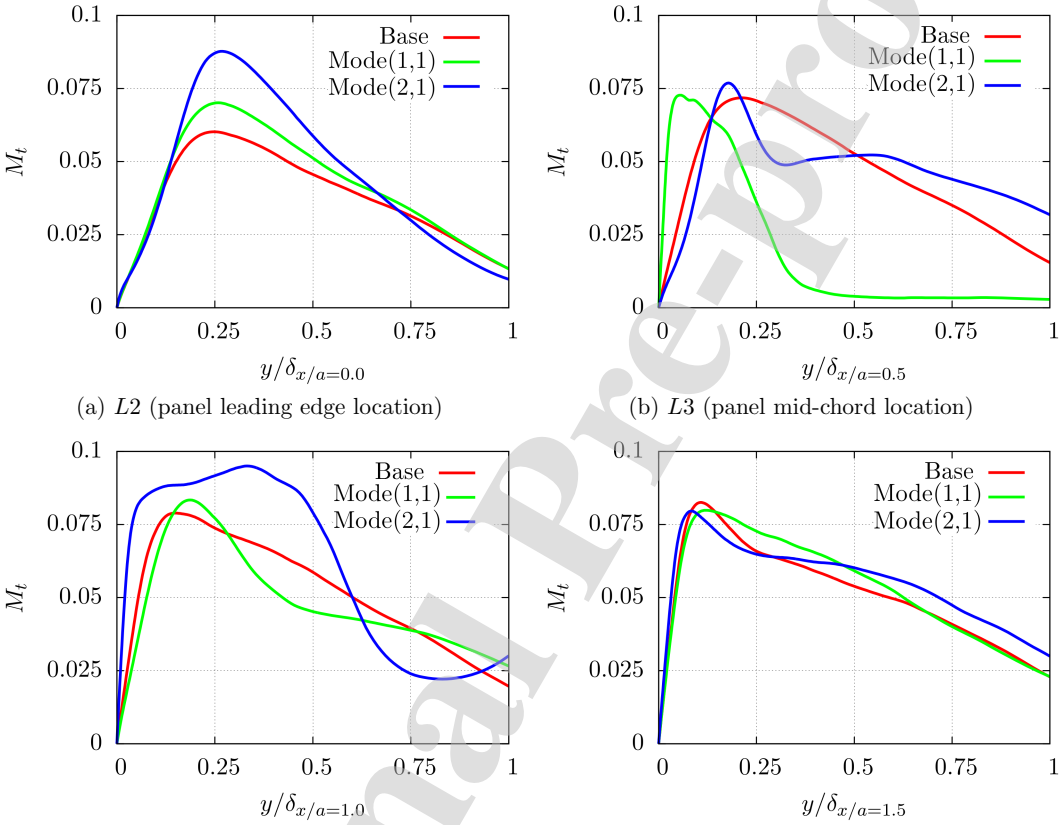

(a) $L2$ (panel leading edge location)

(b) $L3$ (panel mid-chord location)

(c) $L4$ (panel trailing edge location)

(d) $L5$ (a downstream location)

Figure 8: Turbulent Mach number (M_t) wall normal profiles for the three cases at (a) the leading edge of panel (b) at the center of panel (c) at the trailing edge of panel and (d) at $x/a = 1.5$ on the surface and at $z/a = 0$. For locations detail refer Table 2.

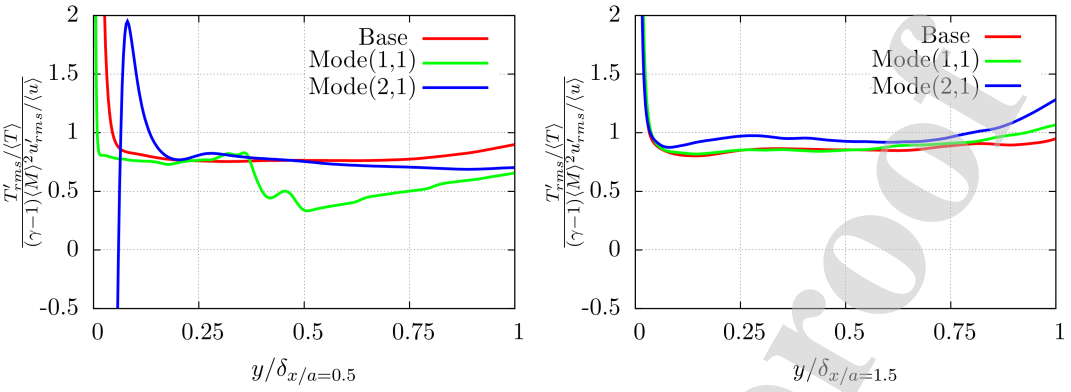

(a) $L3$ (panel mid-chord location) (b) $L5$ (a downstream location)

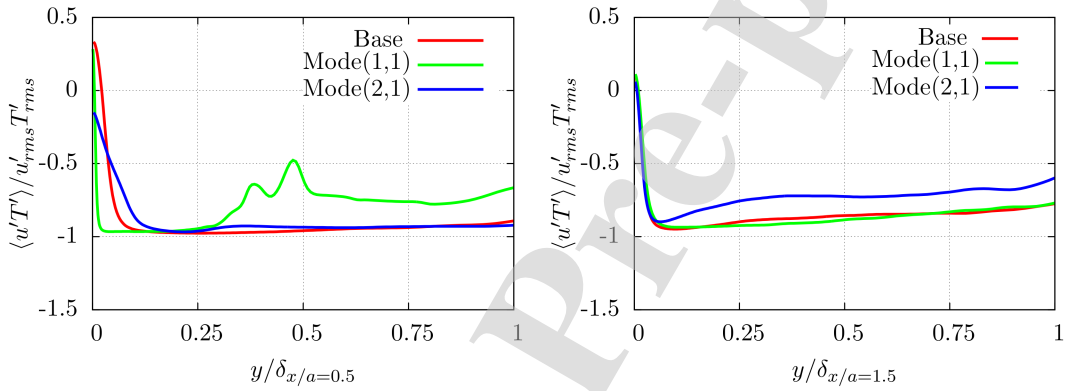

(c) $L3$ (panel mid-chord location) (d) $L5$ (a downstream location)

Figure 9: Applicability of the strong Reynolds analogy for the three cases. (a) Eq. 18 at $x/a = 0.5$ (b) Eq. 18 at $x/a = 1.5$ (c) Eq. 19 at $x/a = 0.5$ (d) Eq. 19 at $x/a = 1.5$

temperature fluctuations for adiabatic walls leads to the strong Reynolds analogy (SRA).

$$\frac{T'_{rms}}{\langle T\rangle} = (\gamma-1)\langle M\rangle^2 \frac{u'_{rms}}{\langle u\rangle} \tag{18}$$

$$\frac{\langle u'T'\rangle}{u'_{rms}T'_{rms}} = -1, \tag{19}$$

The simulations specify $Pr = 0.72$ for air, which affects the underlying assumption. Nonetheless, the application of the SRA greatly aids analysis and motivates an examination of its accuracy in the presence of the surface deformation. The SRA relation of Eq. 18 is examined at two streamwise locations: the panel mid-chord location $L3$ and downstream location $L5$ at $x/a = 1.5$ in Fig. 9(a) and Fig. 9(b) respectively. The figures display the ratio $(T'_{rms}/\langle T\rangle)/\big((\gamma-1)\langle M\rangle^2 u'_{rms}/\langle u\rangle\big)$ as a function of the wall distance (y/δ_x) with deviations from unity being the primary consideration. For the Base case, the ratio remains nearly constant at ≈ 0.8 for most of the boundary layer ($0.05 \lessapprox y/\delta_{x/a=0.5} \lessapprox 1$) at both the mid-chord and downstream locations ($L3$ and $L5$), closely following the SRA. However, in the close vicinity of the wall for $y/\delta_x \lessapprox 0.06$, the left hand side (LHS) of Eq. 18 becomes significantly higher compared to the right hand side (RHS), indicating the dominance of thermal effects. In the presence of surface deformations, the ratio of LHS to

RHS of Eq. 18 reduces to a minimum of ≈ 0.35 for Mode(1,1) between $0.35 \lessapprox y/\delta_{x/a=0.5} \lessapprox 1$ as shown in Fig. 9(a); whereas for Mode(2,1), it drops significantly in the near-wall region for $y/\delta_{x/a=0.5} \lessapprox 0.06$ due to the negative streamwise velocity inside the flow separation. Nevertheless, at the downstream location $L5$, the boundary layer for both Mode(1,1) and Mode(2,1) returns to the Base case profile, confirming the SRA in most of the boundary layer (Fig. 9 b).

Similarly the second SRA relation, Eq. 19), is evaluated for the three cases. The normalized thermal shear stress, $\langle u'T' \rangle / u'_{rms} T'_{rms}$, for increasing wall normal distance is displayed in Fig. 9(c) and Fig. 9(d) for location $L3$ and $L5$ respectively. As anticipated, the anti-correlation between the velocity and thermal fluctuations is evident for all the three cases at the panel mid-chord and downstream locations. The correlation profile for Mode(1,1) (Fig. 9 c) at the upstream location $L3$ exhibits higher values (or lower negative values) as high as -0.5 for the wall distance in $0.25 \lessapprox y/\delta_{x/a=0.5} \lessapprox 1$ compared to the Base case and Mode(2,1). The anti-correlations between the velocity and temperature, for all cases, drop sharply to near-zero values in the near-wall region ($y/\delta_x \lessapprox 0.1$), as shown in Fig. 9(c) and Fig. 9(d).

3.3. Effects on turbulence structure

We now examine the effect of surface deformation on the evolution of coherent structures. Their descriptions, including jet- and wake-like structures [7] or near-wall streamwise streaks [54] may be characterized by different length scales. The turbulent eddies from the outer region of the boundary layer influence the near wall streaks, whose imprints on the wall may be examined in terms of the coherent wall pressure fluctuations. The effect of compressibility on these structures is significant; for example, the streaks are known to be relatively smaller in size compared to their incompressible counterparts [55].

The two-point cross-correlation is typically employed to extract turbulent scales of interest:

$$\langle \phi'_L \psi' \rangle = \frac{\langle \phi'(\vec{x}_L) \psi'(\vec{x}_L + \vec{\Delta x}) \rangle}{\phi_\infty \psi_\infty}, \tag{20}$$

where ϕ' and ψ', are two representative variables, $\vec{x}_L$ is a specific chosen location in the flow (Table 2), $\vec{\Delta x}$ represents the separation between the two points and the normalization employs global reference values of the two variables. The two-point correlations between the turbulent wall-pressure and flow pressure for locations $L3$ and $L4$ are displayed in Fig. 10 for the three cases. The correlation $\langle p'_{L3} p' \rangle / p^2_\infty$ in xz and xy planes on the flat surface (Base case) is displayed in Fig. 10(a) and Fig. 10(b) respectively, while its evolution at the downstream location $L4$ is displayed in xy plane in Fig. 10(c). The turbulent wall pressure p'_{L3} exhibits positive correlation with the surrounding turbulent wall pressure; in addition, it displays two lobes of negative correlation, one upstream and another downstream of the positive lobe, along the flow direction as shown in Fig. 10(a). The streamwise and spanwise extents of the correlation are $\approx 0.15a$ ($\approx 4.06\delta_{x/a=0.5}$) and $\approx 0.075a$ ($\approx 2.03\delta_{x/a=0.5}$) respectively, whereas in the wall normal direction (Fig. 10b) the correlation extends up to $\approx 0.04a$ ($\approx 1.08\delta_{x/a=0.5}$) from the wall, leading to three-dimensional cones of the positive and negative correlations. The approximate base diameters for the positive and negative cones of the pressure correlations are $0.075a$ ($\approx 2.03\delta_{x/a=0.5}$) and $0.0167a$ ($\approx 0.45\delta_{x/a=0.5}$) respectively. The size of the correlation, $\langle p'_{L4} p' \rangle / p^2_\infty$, in the wall normal direction at the downstream location $L4$ increases to $0.05a$ ($\approx 1.24\delta_{x/a=1.0}$). This increase of about $\approx 25\%$ occurs for the complete 3-D correlation, when compared to $\approx 10\%$ increase of the the boundary layer thickness from location $L3$ to location $L4$. These correlations are integrally connected with various near wall dynamics on length-scales and flow structure orientations as discussed by Na and Moin [56], Sillero et al. [57], Shinde et al. [58] for incompressible turbulent boundary layers.

The boundary layer undergoes modifications due to the presence of surface deformations, as discussed in Sec. 3.1; in the same vein, the two-point turbulent pressure correlations are also modified. The effects of surface deflection on the correlations at locations $L3$ and $L4$ for Mode(1,1) and Mode(2,1) are displayed in Figs. 10(d),(e),(f) and Figs. 10(g),(h),(i) respectively. For Mode(1,1), the turbulent pressure correlation $\langle p'_{L3} p' \rangle / p^2_\infty$ at $L3$ (Fig. 10d) is, relatively, weak compared to the Base case (Fig. 10a); whereas its dimensions and shape appear nearly the same, in the absolute sense. However, the boundary layer height at this location $\delta_{x/a=1.0}$ decreases by $\approx 66\%$ compared to the Base case. At the downstream location $L4$, the size of the

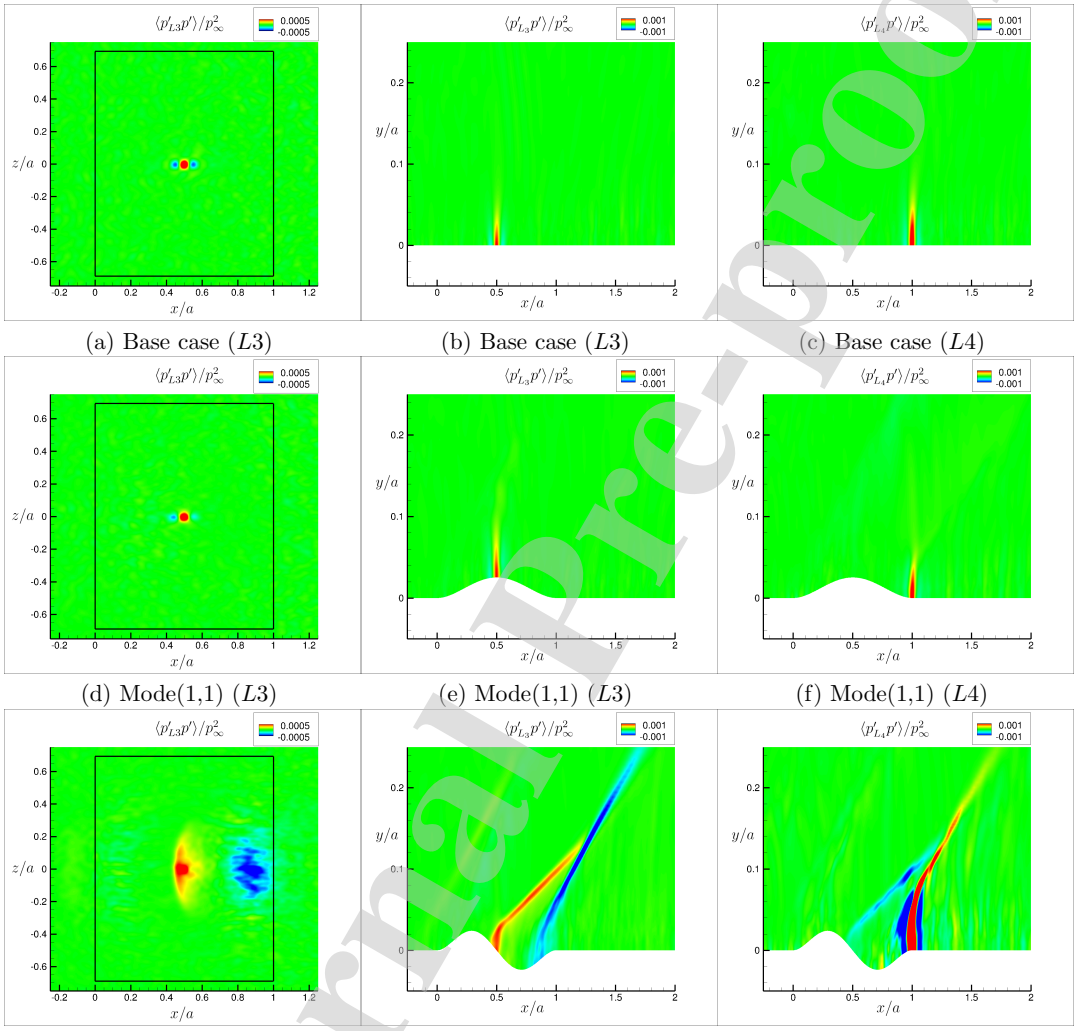

(a) Base case ($L3$) (b) Base case ($L3$) (c) Base case ($L4$)

(d) Mode(1,1) ($L3$) (e) Mode(1,1) ($L3$) (f) Mode(1,1) ($L4$)

(g) Mode(2,1) ($L3$) (h) Mode(2,1) ($L3$) (i) Mode(2,1) ($L4$)

Figure 10: Two-point turbulent pressure correlations at $L3$ (panel mid-chord) and $L4$ (panel trailing edge) locations (Table 2) for the flat and deflected surfaces.

conical pressure correlation increases by ≈ 10%, making an inclination of ≈ 20 deg to the wall normal, as shown in Fig. 10(f)[1]; while the boundary layer height at this location becomes ≈ 98.5% of that in the Base case.

For Mode(2,1) surface deflection, the two-point pressure correlations (Eq. 20) at the two locations $L3$ and $L4$ are significantly modified compared to the Base case, as shown in Figs. 10(g),(h) and (i). Unlike Mode(1,1), the location $L3$ for Mode(2,1) lies in the separation region (Fig. 5 c, $x/a = 0.5$), in the mean sense; thus the wall pressure fluctuations exhibit a much larger extent of the correlation compared to the Base case and Mode(1,1), which is in agreement with the observations of Shinde et al. [58]. Furthermore, the separation region of Mode(2,1) is accompanied by the presence of a set of expansion and compression waves that emanate near the locations $L3$ and $L4$ respectively, which results in bridging the turbulent flow structures at the two locations. Consequently, the turbulent wall pressure at location $L3$ manifests a strong correlation with the pressure fluctuations near location $L4$, albeit an anti-correlation. The positive correlation near location $L3$ spans over $\approx 0.15a$ ($\approx 3.34\delta_{x/a=0.5}$) and $\approx 0.4a$ ($\approx 8.9\delta_{x/a=0.5}$) in the streamwise and spanwise directions respectively (Fig. 10g). In addition, an equally strong negative correlation manifests at a downstream location of $x/a = 0.85$, spanning over $\approx 0.2a$ ($\approx 4.46\delta_{x/a=0.5}$) and $\approx 0.4a$ ($\approx 8.9\delta_{x/a=0.5}$) in the streamwise and spanwise directions respectively (Fig. 10g). Interestingly, the pressure correlation at $L3$ escalates due to expansion and compression waves and extends into the far field, engaging the large scales of turbulence (Fig. 10h). Similarly, the turbulent wall pressure at $L4$ exhibits an anti-correlation with location $L3$, stretching the correlation into the far field, as shown in Fig. 10(i).

The effect of surface deformation on the structure of turbulence is estimated with Lumley's traceless and symmetric tensor that identifies deviation from isotropic turbulence[59]:

$$a_{ij} = \frac{\langle u_i' u_j' \rangle}{2\mathcal{K}} - \frac{\delta_{ij}}{3}, \tag{21}$$

where $\mathcal{K} = \langle u_i' u_i' \rangle / 2$ is the turbulent kinetic energy and δ_{ij} is the Kronecker delta. For reference, the second and third scalar invariants that aid in the deviation assessments are [60]:

$$II = a_{ij}a_{ji} = \frac{1}{2}a_{ii}^2 \quad \text{and} \quad III = a_{ij}a_{jk}a_{ki} = \frac{1}{3}a_{ii}^3 \tag{22}$$

respectively, since variant I is zero. The invariant-map, plotted as III versus II map, manifests a triangular shape (Lumley's triangle), which includes all physically realizable states of turbulence inside the triangle.

The turbulence anisotropy invariant-maps for the three cases (Base case, Mode(1,1) and Mode(2,1)) at four streamwise locations, namely $L2$, $L3$, $L4$, and $L5$ (refer Table 2), are displayed in Figs. 11(a),(b),(c), and (d), respectively, where the black curves delineate Lumley's triangle. In each sub-figure (of Fig. 11), the invariants of the anisotropy tensor are estimated along the wall normal direction for the three cases. The curves for the Base case, Mode(1,1) and Mode(2,1) are shown using square, triangle and circle symbols respectively, colored using the wall normal distance normalized by the local boundary layer thickness. The arrows indicate the direction of increasing wall normal distance. In general, the curves begin (near wall) in the left corner of the triangle. In this region, the streamwise and spanwise components are similar (two-component limit), and are much larger than the wall-normal velocity fluctuation component. As the wall normal distance increases, invariants II and III increase together in somewhat linear fashion and the curve forms the upper corner; this is the one-component limit where one component (here, the streamwise component) is much larger than the other two components. With further distance from the surface, both III and II decrease to finally yield the three-component limit or the isotropic turbulence at the bottom corner of the triangle, where the II and III invariants become zero.

The near-wall turbulence at the panel leading edge (location $L2$) for Mode(1,1) and Mode(2,1) differs from the Base case in terms of the starting (near-wall) values of the invariants, initiating at points far from the two-components limit, as displayed in Fig. 11(a). The onset/presence of flow separation at location $L2$ appears to have influenced the near-wall turbulence structure for Mode(1,1) and Mode(2,1). However, the

[1]The axes of Fig. 10 use different scales for better comparison among the three cases.

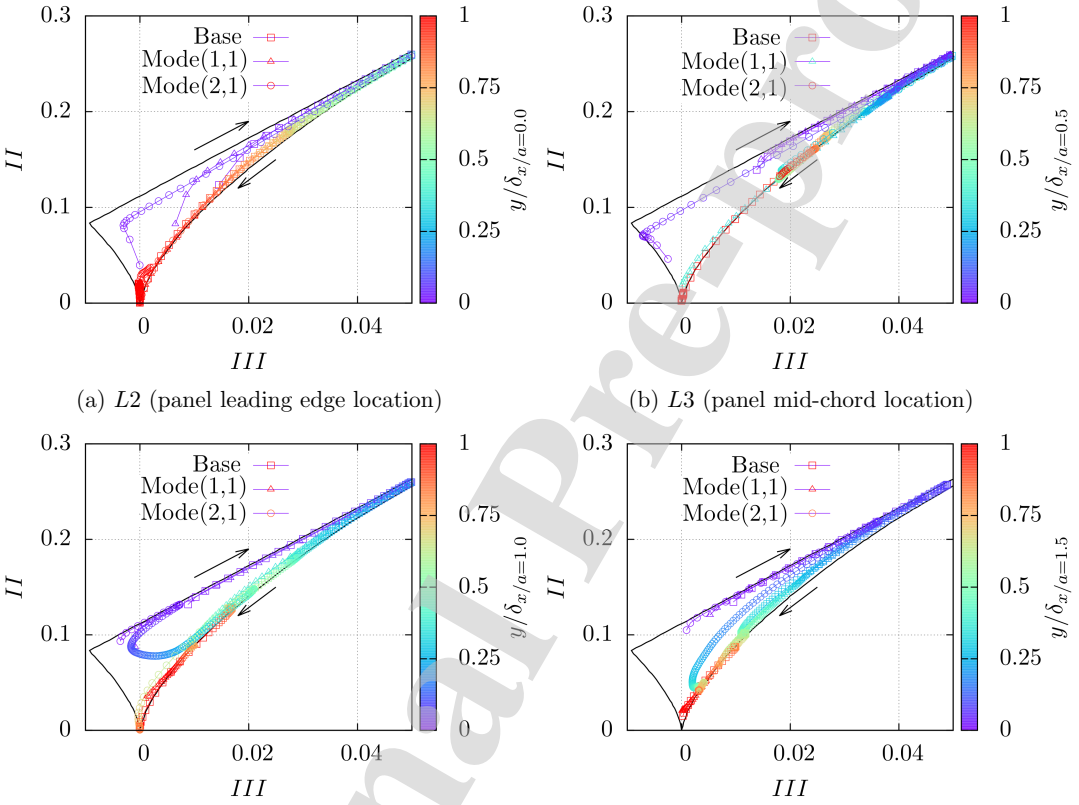

(a) $L2$ (panel leading edge location)

(b) $L3$ (panel mid-chord location)

(c) $L4$ (panel trailing-edge location)

(d) $L5$ (a downstream location)

Figure 11: Turbulence anisotropy map for Base case, Mode(1,1) and Mode(2,1) at different streamwise locations. The black curves delineate Lumley's triangle.

one-component limit for the three cases is reached at about $y \approx 0.25\delta_{x/a=0.0}$, in addition to the similar behavior for $y/\delta_{x/a=0.0} \gtrapprox 0.25$ (Fig. 11a). At location $L3$, the anisotropy invariant-curves for the Base case and Mode(1,1) follow the two-components limit and one-component limit, eventually reaching the isotropy limit (Fig. 11 b). In contrast, the near-wall turbulence state for Mode(2,1) indicates the influence of the flow separation at this location ($L3$), without reaching the isotropy limit at $y/\delta_{x/a=1.0} = 1$, where the flow field undergoes an expansion. The similarities and differences of the state of turbulence at this location ($L3$) among the three cases are consistent with the two-point turbulent pressure correlations discussed before. The turbulent anisotropy state at the panel trailing edge (location $L4$) manifests similar behavior for the Base case and Mode(1,1), where the curves follow the typical anisotropy limits; however, the invariant-curve for Mode(2,1) exhibits a jump from the two-components limit in the near wall region to the axisymmetric turbulence expansion path to isotropic turbulence, as displayed in Fig. 11(c). The anisotropy invariant-curves at the downstream location $L5$ for the three cases are shown in Fig. 11(d), where the boundary layer turbulence for Mode(1,1), to large extent, returns to the relaxed state close to the Base line, whereas Mode(2,1) turbulence anisotropy profiles exhibit some deviation, particularly in the outer boundary layer region.

3.4. Flow unsteadiness and turbulence spectra

The surface deformations in Mode(1,1) and Mode(2,1) locally modify the supersonic TBL in terms of the flow properties and turbulence structure, in the time-mean sense, where, as noted before, the modified boundary layer returns to an equilibrium state at about $0.5a$ ($20\delta_{in}$) downstream of the panel trailing edge. However, the surface deformations in some regions introduce a strong adverse pressure gradient, leading to flow separation. For example, the flow near the panel leading edge (location $L2$) for Mode(1,1) and Mode(2,1) as well as near the mid-chord length (location $L3$) separates, transiently but not in the mean sense for the former, due to the adverse pressure gradients, as discussed before in terms of the skin-friction coefficient (Fig. 5c). The regions exhibiting the flow compression and expansion due the surface deformations of Mode(1,1) and Mode(2,1) alongside the Base flow are displayed in Fig. 12, where the density increase due to the compression and decrease due to the expansion are evident. The figure also manifests the increased levels of flow turbulence downstream of the surface deformations for both Mode(1,1) (Fig. 12b) and Mode(2,1) (Fig. 12c) compared to the flat Base case (Fig. 12a), which is consistent with the higher Reynolds stresses in Fig. 7 for the two cases (Mode(1,1), Mode(2,1)).

The turbulence modification in the near wall region due to the surface deformations and flow separation is also analyzed by using the power spectral densities (PSD) of the streamwise velocity and wall pressure. The spectra are computed as a function of the spanwise wavenumber ($\omega_z = 2\pi/\lambda_z$, where λ_z is the wavelength) at the leading ($L2$) and trailing ($L4$) edge locations of the panel, while the streamwise velocity spectra are computed at a wall normal distance of $\approx 0.21\delta_{in}$. The pre-multiplied spectra of the streamwise velocity (E_{uu}) as a function of the spanwise wavenumber (ω_z) for the three cases at the panel leading edge location $L2$ are shown in Fig. 13(a); while the evolution of spectra at the downstream location $L4$ is displayed in Fig. 13(b). The wavenumber and PSD are normalized by using the panel length (a) and free-stream pressure p_∞, respectively. Overall, the spectral energy at the downstream location $L4$ is higher for all wavenumbers, where both (the upstream $L2$ and downstream $L4$) spectra exhibit a short production range ($E_{uu} \propto \omega_z^{-1}$) that is centered around $\omega_z \approx 100$. This wavenumber corresponds to a spanwise wavelength scale of $\lambda_z \approx 0.063a$ ($\lambda_z = 2.5\delta_{in}$). Furthermore, the streamwise velocity spectra exhibit a very short inertial sub-range of turbulence at the both locations, as indicated by the solid black line with $\omega_z E_{uu} \propto \omega_z^{-2/3}$ (*i.e.* $E_{uu} \propto \omega_z^{-5/3}$). As opposed to the velocity spectra for Base case, the magnitudes of PSD for Mode(1,1) and Mode(2,1) are higher at the lower wavenumbers, as shown in Figs. 13(a) and (b), which correspond to the flow three-dimensionality induced by the surface deformations.

A flat region of a pre-multiplied spectrum of the wall pressure represents the ω_z^{-1} dependence of the wall pressure PSD on the wavenumber/frequency. In this range of wavenumbers, the pressure contribution is mainly due to the large eddies from the log-layer [61], which corresponds to the mid-range wavenumbers/frequencies of the pressure spectra (Figs. 13c and d). The magnitudes of wall pressure PSD at downstream location $L4$ are, to some degree, higher compared to upstream location $L2$ for all wavenumbers, as

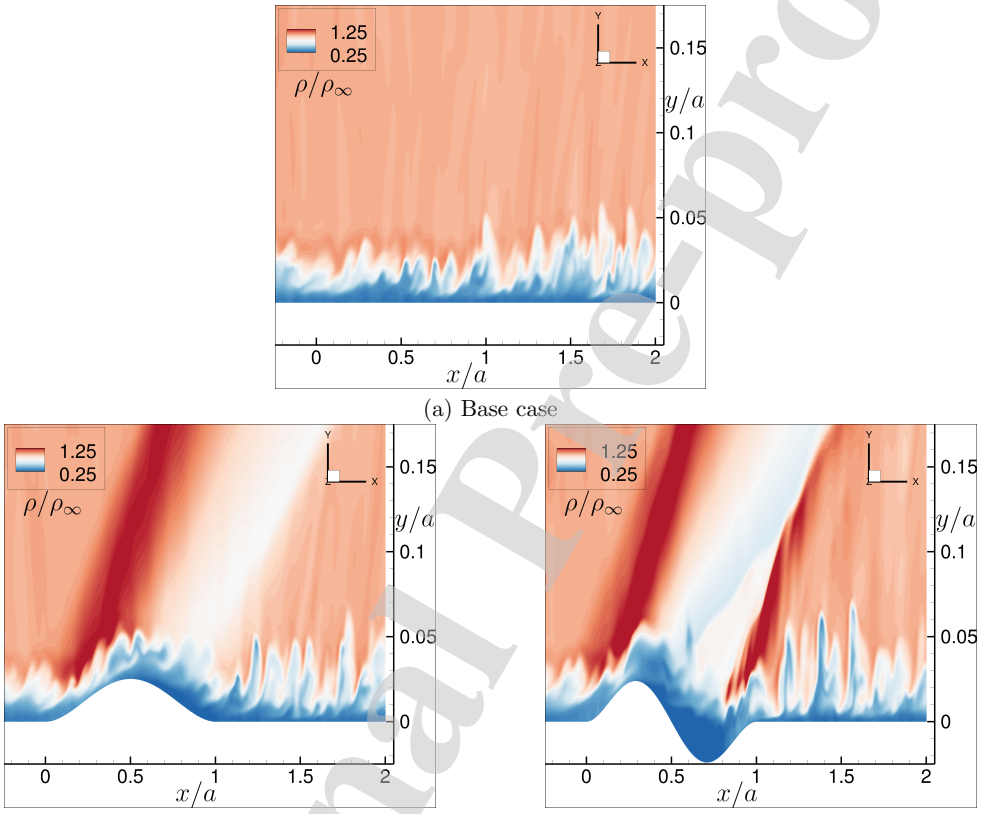

(a) Base case

(b) Mode(1,1)

(c) Mode(2,1)

Figure 12: Normalized density at the mid-span ($z = 0$) plane for the three cases. (a) flat surface Base case (b) Mode(1,1) surface deformation (c) Mode(2,1) surface deformation.

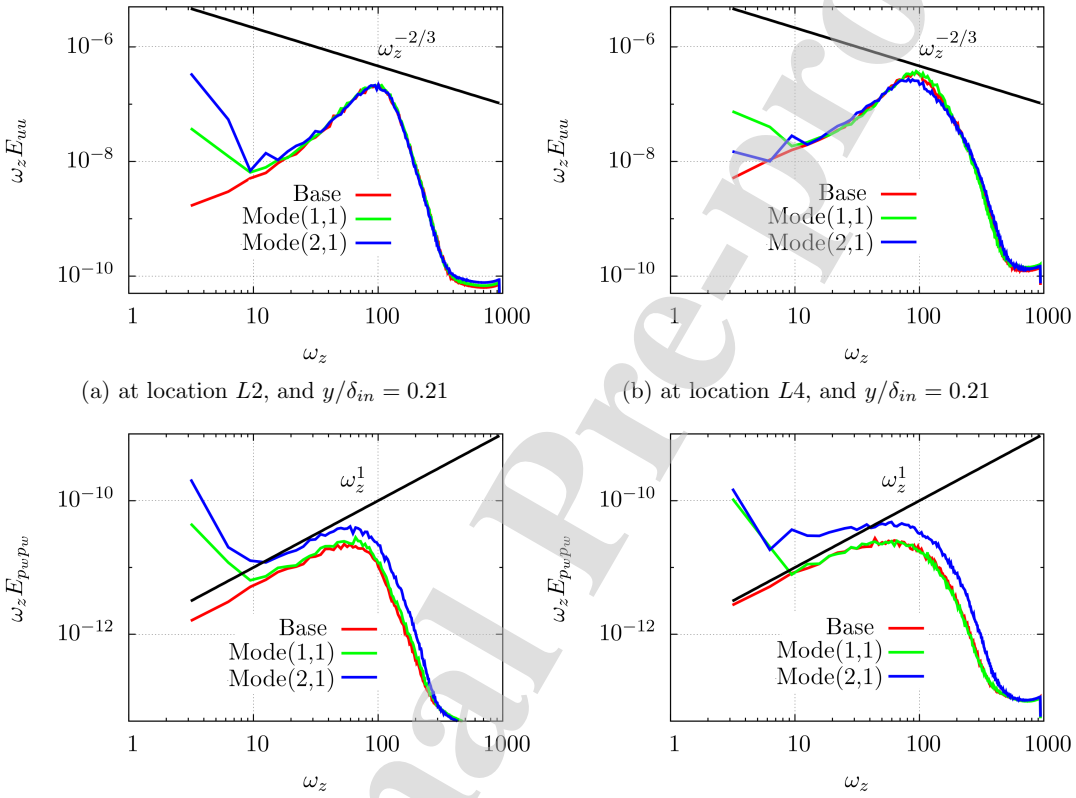

(a) at location $L2$, and $y/\delta_{in} = 0.21$

(b) at location $L4$, and $y/\delta_{in} = 0.21$

(c) at location $L2$, and $y/\delta_{in} = 0.0$

(d) at location $L4$, and $y/\delta_{in} = 0.0$

Figure 13: Turbulence spectra of the streamwise velocity and wall pressure versus the spanwise wavenumber for the three cases. (a) Streamwise velocity spectra at the panel leading edge and $y/\delta_{in} = 0.21$ (b) streamwise velocity spectra at the panel trailing edge and $y/\delta_{in} = 0.21$ (c) wall pressure spectra at the panel leading edge and $y/\delta_{in} = 0.0$ (c) wall pressure spectra at the panel trailing edge and $y/\delta_{in} = 0.0$.

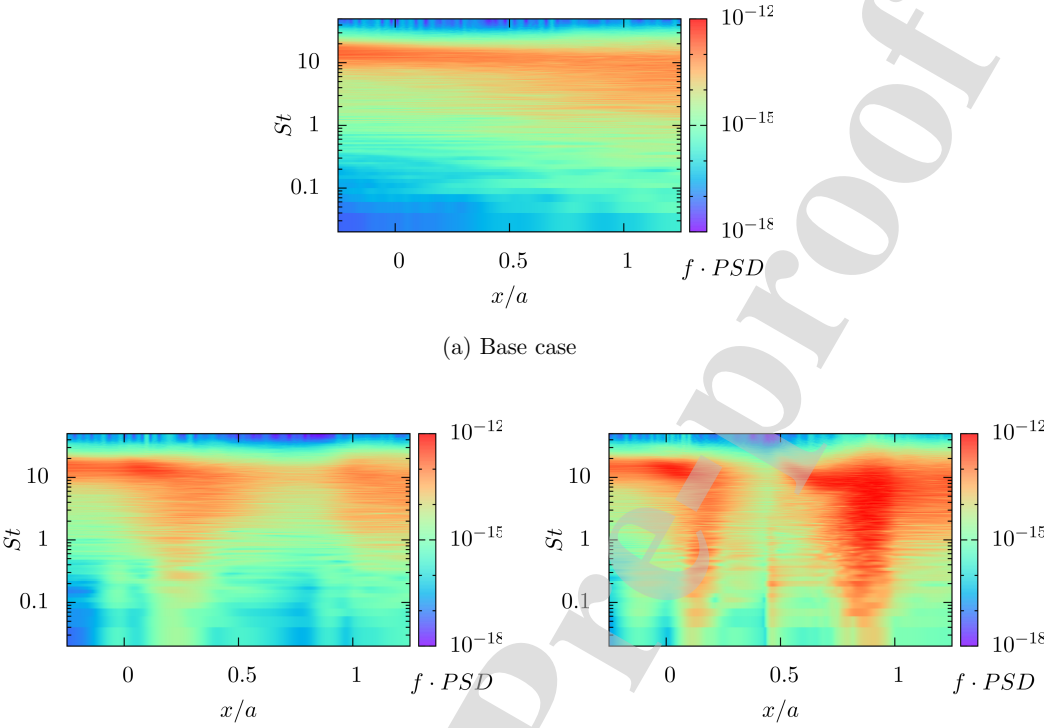

(a) Base case

(b) Mode(1,1)

(c) Mode(2,1)

Figure 14: Pre-multiplied power spectral density of the wall pressure at $z = 0$

shown in Figs. 13(c) and (d). Additionally, the flat range of the pre-multiplied spectrum ($\omega_z E_{p_w p_w} \propto \omega_z^0$, Fig. 13c) at $L2$ is increased at the downstream location $L4$ (Fig. 13d). At the lower wavenumbers however, the wall pressure spectra do not exhibit ω_z^2 power law, or equivalently ω_z^3 for the pre-multiplied spectra, as shown in Figs. 13(c) and (d); rather that manifest no dependence on the wavenumber, *i.e.* $E_{p_w p_w} \propto \omega_z^0$ (or $\omega_z E_{p_w p_w} \propto \omega_z^1$), agreeing with the experimental observation of Beresh et al. [62]. Similar to the streamwise velocity spectra, the wall pressure spectra for Mode(1,1) and Mode(2,1) exhibit higher spectral energy for the lower wavenumbers at both locations $L2$ and $L4$ (Fig. 13c and d) when compared to the flat surface Base case spectra.

In addition to the increased level of turbulence, the flow separation associated with the shock wave boundary layer interaction (SWBLI) introduces a characteristic low-frequency unsteadiness [63, 37, 64]. The low frequencies are 1 to 2 orders of magnitude lower compared to the turbulence frequencies, whose potential origin mechanisms have been discussed in Clemens and Narayanaswamy [65]. The pre-multiplied wall pressure PSD of the temporal data along the center-line ($z = 0$) for the three cases are displayed in Fig. 14. As opposed to the Base case wall pressure PSD (Fig. 14a), the wall pressure spectra for Mode(1,1) (Fig. 14 b) and Mode(2,1) (Fig. 14 c) clearly manifest the presence of low-frequency unsteadiness, prominently in the regions where the flow undergoes separation, that is, in the proximity of location $L2$ ($x/a \approx 0.0$) for Mode(1,1) and locations $L2$ and $L4$ ($x/a \approx 1.0$) for Mode(2,1). The frequencies are normalized by using the panel length (a) and free-stream velocity (u_∞), leading to Strouhal numbers ($St = f u_\infty / a$) of the order of those observed in SBLI (as low as 0.02), particularly for Mode(1,1) and Mode(2,1). Furthermore, the

magnitudes of wall pressure spectra increase due to the surface deformations (Fig. 14) for almost all Strouhal numbers ($0.02 \leq St \lessapprox 40$), indicating an increased level of flow turbulence in addition to the low frequency dynamics.

4. Conclusion

We have examined the effects of surface modal deformations on a spatially evolving supersonic turbulent boundary layer. Although the surface deformations manifest minimal thermal and compressibility effects on the flow in terms of the Morkovin's hypothesis and strong Reynolds analogy, they result in local modification of the turbulence structure as well as, in general, amplification of the flow turbulence. The rapid distortion theory, turbulence anisotropy maps, and turbulent two point correlations elucidate the effects of surface deflections on the boundary layer in terms of the length and time scales, anisotropy and structure of turbulence. The adverse pressure gradients induced by the surface deformations cause flow separation, giving rise to the low frequency dynamics associated with the shock wave boundary layer interaction. For the parameters considered, the surface deflection associated with Mode(2,1) impacts the TBL far more than that associated with Mode(1,1); this is mainly due to the higher degree of flow separation induced by the Mode(2,1) surface deflection. Thus from the fluid-thermal-structural-interaction (FTSI) point of view, an initial static surface deformation caused by, for instance, thermal loading at high-speeds can lead to the low-frequency flow dynamics (pressure loading); which can eventually result in a coupled fluid-structure interaction (FSI) and in turn a full FTSI. In future, we will extend the present investigation to a fully coupled spontaneous FSI/FTSI alongside a strong impinging oblique shock wave.

Acknowledgments

The authors express gratitude to the Air Force Office of Scientific Research (AFOSR) (Monitor: Dr. S. Popkin) and the Collaborative Center for Aeronautical Sciences (CCAS). This material is based on research partially sponsored by the U.S. Air Force under agreement number FA865019-2-2204. The U.S. Government is authorized to reproduce and distribute reprints for Governmental purposes notwithstanding any copyright notation thereon. The simulations were performed with grants of computer time from the DoD HPCMP and the Ohio Supercomputer Center. Some figures have been made with complimentary licenses of FieldView obtained from Intelligent Light under the University Partners Program.

References

1. Bradshaw P. Compressible turbulent shear layers. *Annual Review of Fluid Mechanics* 1977;9(1):33–52.
2. Dussauge J, Gaviglio J. The rapid expansion of a supersonic turbulent flow: role of bulk dilatation. *Journal of Fluid Mechanics* 1987;174:81–112.
3. Spina EF, Smits AJ, Robinson SK. The physics of supersonic turbulent boundary layers. *Annual Review of Fluid Mechanics* 1994;26(1):287–319.
4. Lele SK. Compressibility effects on turbulence. *Annual review of fluid mechanics* 1994;26(1):211–54.
5. Guarini SE, Moser RD, Shariff K, Wray A. Direct numerical simulation of a supersonic turbulent boundary layer at mach 2.5. *Journal of Fluid Mechanics* 2000;414:1–33.
6. Foysi H, Sarkar S, Friedrich R. Compressibility effects and turbulence scalings in supersonic channel flow. *Journal of Fluid Mechanics* 2004;509:207–16.
7. Pirozzoli S, Bernardini M. Turbulence in supersonic boundary layers at moderate reynolds number. *Journal of Fluid Mechanics* 2011;688:120–68.
8. Smits AJ, Dussauge JP. Turbulent shear layers in supersonic flow. Springer Science & Business Media; 2006.
9. Morkovin MV. Effects of compressibility on turbulent flows. *Mécanique de la Turbulence* 1962;367:380.
10. Bradshaw P. The effect of mean compression or dilatation on the turbulence structure of supersonic boundary layers. *Journal of Fluid Mechanics* 1974;63(3):449–64.
11. Gaviglio J. Reynolds analogies and experimental study of heat transfer in the supersonic boundary layer. *International journal of heat and mass transfer* 1987;30(5):911–26.
12. Fernando EM, Smits AJ. A supersonic turbulent boundary layer in an adverse pressure gradient. *Journal of Fluid Mechanics* 1990;211:285–307.
13. Wang X, Wang Z, Sun M, Wang Q, Hu Z. Effects of favorable pressure gradient on turbulence structures and statistics of a flat-plate supersonic turbulent boundary layer. *Physics of Fluids* 2020;32(2):025107.

14. Williams OJ, Sahoo D, Baumgartner ML, Smits AJ. Experiments on the structure and scaling of hypersonic turbulent boundary layers. *Journal of Fluid Mechanics* 2018;834:237–70.
15. Duan L, Choudhari MM, Zhang C. Pressure fluctuations induced by a hypersonic turbulent boundary layer. *Journal of Fluid Mechanics* 2016;804:578–607.
16. Zhang C, Duan L, Choudhari MM. Effect of wall cooling on boundary-layer-induced pressure fluctuations at mach 6. *Journal of Fluid Mechanics* 2017;822:5–30.
17. Wang QC, Wang ZG, Sun MB, Yang R, Zhao YX, Hu Z. The amplification of large-scale motion in a supersonic concave turbulent boundary layer and its impact on the mean and statistical properties. *Journal of Fluid Mechanics* 2019;863:454–93.
18. Wang Qc, Wang Zg. Structural characteristics of the supersonic turbulent boundary layer subjected to concave curvature. *Applied Physics Letters* 2016;108(11):114102.
19. Donovan JF, Spina EF, Smits AJ. The structure of a supersonic turbulent boundary layer subjected to concave surface curvature. *Journal of Fluid Mechanics* 1994;259:1–24.
20. Sun M, Sandham ND, Hu Z. Turbulence structures and statistics of a supersonic turbulent boundary layer subjected to concave surface curvature. *Journal of Fluid Mechanics* 2019;865:60–99.
21. Spalart PR, Watmuff JH. Experimental and numerical study of a turbulent boundary layer with pressure gradients. *Journal of Fluid Mechanics* 1993;249:337–71.
22. Tichenor N, Humble R, Bowersox R. Response of a hypersonic turbulent boundary layer to favourable pressure gradients. *Journal of Fluid Mechanics* 2013;722:187–213.
23. Wang Qc, Wang Zg, Zhao Yx. The impact of streamwise convex curvature on the supersonic turbulent boundary layer. *Physics of Fluids* 2017;29(11):116106.
24. Wang Qc, Wang Zg, Zhao Yx. An experimental investigation of the supersonic turbulent boundary layer subjected to concave curvature. *Physics of Fluids* 2016;28(9):096104.
25. Neet MC, Austin JM. Effects of surface compliance on shock boundary layer interaction in the caltech mach 4 ludwieg tube. In: *AIAA Scitech 2020 Forum*. 2020:0816.
26. Beam RM, Warming R. An implicit factored scheme for the compressible navier-stokes equations. *AIAA journal* 1978;16(4):393–402.
27. Visbal M, Gordnier R. Numerical simulation of the interaction of a transitional boundary layer with a 2-d flexible panel in the subsonic regime. *Journal of fluids and structures* 2004;19(7):881–903.
28. Shinde V, McNamara J, Gaitonde D, Barnes C, Visbal M. Transitional shock wave boundary layer interaction over a flexible panel. *Journal of Fluids and Structures* 2019;90:263–85.
29. Shinde V, McNamara J, Gaitonde D. Control of transitional shock wave boundary layer interaction using structurally constrained surface morphing. *Aerospace Science and Technology* 2020;96:105545.
30. Visbal MR, Gaitonde DV. High-order-accurate methods for complex unsteady subsonic flows. *AIAA journal* 1999;37(10):1231–9.
31. Gaitonde DV, Visbal MR. Padé-type higher-order boundary filters for the navier-stokes equations. *AIAA journal* 2000;38(11):2103–12.
32. Visbal MR, Gaitonde DV. On the use of higher-order finite-difference schemes on curvilinear and deforming meshes. *Journal of Computational Physics* 2002;181(1):155–85.
33. Garmann DJ. Characterization of the vortex formation and evolution about a revolving wing using high-fidelity simulation. *Ph D Thesis* 2013;.
34. Visbal M, Gaitonde D. Shock capturing using compact-differencing-based methods. In: *43rd AIAA Aerospace Sciences Meeting and Exhibit*. 2005:1265.
35. Shinde VJ, McNamara JJ, Gaitonde DV. Shock wave turbulent boundary layer interaction over a flexible panel. In: *AIAA Scitech 2021 Forum*. 2021:0488.
36. Shinde VJ, Gaitonde DV, McNamara JJ. Control of transitional shock boundary layer interaction using surface morphing. In: *AIAA Scitech 2019 Forum*. 2019:1895.
37. Shinde V, McNamara J, Gaitonde D. Control of transitional shock wave boundary layer interaction using structurally constrained surface morphing. *Aerospace Science and Technology* 2019;:105545.
38. Shinde VJ, Gaitonde DV, McNamara JJ. Control of shock wave turbulent boundary layer interaction using structurally constrained active surface morphing. In: *AIAA Scitech 2020 Forum*. 2020:0038.
39. Klein M, Sadiki A, Janicka J. A digital filter based generation of inflow data for spatially developing direct numerical or large eddy simulations. *Journal of computational Physics* 2003;186(2):652–65.
40. Xu S, Rempfer D, Lumley J. Turbulence over a compliant surface: numerical simulation and analysis. *Journal of Fluid Mechanics* 2003;478:11–34.
41. Adler MC, Gonzalez DR, Stack CM, Gaitonde DV. Synthetic generation of equilibrium boundary layer turbulence from modeled statistics. *Computers & Fluids* 2018;165:127–43.
42. Bernardini M, Pirozzoli S. Wall pressure fluctuations beneath supersonic turbulent boundary layers. *Physics of Fluids* 2011;23(8):085102.
43. Van Dyke MD. A study of second-order supersonic-flow theory. *National Advisory Committee for Aeronautics* 1951;Technical Notes(2200):1–73.
44. Chauhan KA, Monkewitz PA, Nagib HM. Criteria for assessing experiments in zero pressure gradient boundary layers. *Fluid Dynamics Research* 2009;41(2):021404.
45. Vinuesa R, Örlü R, Vila CS, Ianiro A, Discetti S, Schlatter P. Revisiting history effects in adverse-pressure-gradient turbulent boundary layers. *Flow, turbulence and combustion* 2017;99(3-4):565–87.

46. Sun Mb, Hu Z, Sandham ND. Recovery of a supersonic turbulent boundary layer after an expansion corner. *Physics of Fluids* 2017;29(7):076103.
47. Schlatter P, Örlü R. Turbulent boundary layers at moderate reynolds numbers: inflow length and tripping effects. *Journal of Fluid Mechanics* 2012;710:5.
48. Smith DR, Smits AJ. The effects of successive distortions on a turbulent boundary layer in a supersonic flow. *Journal of Fluid Mechanics* 1997;351:253–88.
49. Smith D, Smits A. A study of the effects of curvature and compression on the behavior of a supersonic turbulent boundary layer. *Experiments in fluids* 1995;18(5):363–9.
50. Townsend A. The structure of turbulent shear flow. *The Structure of Turbulent Shear Flow, by AAR Townsend, pp 440 ISBN 0521298199 Cambridge, UK: Cambridge University Press, March 1980* 1980;:440.
51. Jayaram M, Donovan J, Dussauge JP, Smits A. Analysis of a rapidly distorted, supersonic, turbulent boundary layer. *Physics of Fluids A: Fluid Dynamics* 1989;1(11):1855–64.
52. Ribner HS, Tucker M. Spectrum of turbulence in a contracting stream; vol. 1113. National Advisory Committee for Aeronautics; 1952.
53. Batchelor G, Proudman I. The effect of rapid distortion of a fluid in turbulent motion. *The Quarterly Journal of Mechanics and Applied Mathematics* 1954;7(1):83–103.
54. Ganapathisubramani B, Clemens NT, Dolling D. Large-scale motions in a supersonic turbulent boundary layer. *Journal of fluid Mechanics* 2006;556:271–82.
55. Martín MP. Direct numerical simulation of hypersonic turbulent boundary layers. part 1. initialization and comparison with experiments. *Journal of Fluid Mechanics* 2007;570:347–64.
56. Na Y, Moin P. Direct numerical simulation of a separated turbulent boundary layer. *Journal of Fluid Mechanics* 1998;374:379–405.
57. Sillero JA, Jiménez J, Moser RD. Two-point statistics for turbulent boundary layers and channels at reynolds numbers up to $\delta^+ \approx 2000$. *Physics of Fluids* 2014;26(10):105109.
58. Shinde VJ, Laval JP, Stanislas M. Effect of mean pressure gradient on the turbulent wall pressure–velocity correlations. *Journal of Turbulence* 2014;15(12):833–56.
59. Lumley JL. Computational modeling of turbulent flows. In: *Advances in applied mechanics*; vol. 18. Elsevier; 1979:123–76.
60. Pope S, Pope SB. Turbulent Flows. Cambridge University Press; 2000.
61. Bradshaw P. 'inactive'motion and pressure fluctuations in turbulent boundary layers. *Journal of Fluid Mechanics* 1967;30(2):241–58.
62. Beresh SJ, Henfling JF, Spillers RW, Pruett BO. Fluctuating wall pressures measured beneath a supersonic turbulent boundary layer. *Physics of Fluids* 2011;23(7):075110.
63. Delery JM. Shock wave/turbulent boundary layer interaction and its control. *Progress in Aerospace Sciences* 1985;22(4):209–80.
64. Gaitonde DV. Progress in shock wave/boundary layer interactions. *Progress in Aerospace Sciences* 2015;72:80–99.
65. Clemens NT, Narayanaswamy V. Low-frequency unsteadiness of shock wave/turbulent boundary layer interactions. *Annual Review of Fluid Mechanics* 2014;46:469–92.

CONFLICT OF INTEREST STATEMENT

Manuscript title: _____

_____

_____

The authors whose names are listed immediately below certify that they have NO affiliations with or involvement in any organization or entity with any financial interest (such as honoraria; educational grants; participation in speakers' bureaus; membership, employment, consultancies, stock ownership, or other equity interest; and expert testimony or patent-licensing arrangements), or nonfinancial interest (such as personal or professional relationships, affiliations, knowledge or beliefs) in the subject matter or materials discussed in this manuscript.

Author names:

The authors whose names are listed immediately below report the following details of affiliation or involvement in an organization or entity with a financial or nonfinancial interest in the subject matter or materials discussed in this manuscript. Please specify the nature of the conflict on a separate sheet of paper if the space below is inadequate.

Author names:

This statement is signed by all the authors to indicate agreement that the above information is true and correct (*a photocopy of this form may be used if there are more than 10 authors***):**

Author's name (typed)	Author's signature	Date